Advances in Nano Research, *Vol. 16, No. 3 (2024) 231-249*
https://doi.org/10.12989/anr.2024.16.3.231

The efficient data-driven solution to nonlinear continuum thermo-mechanics behavior of structural concrete panel reinforced by nanocomposites: Development of building construction in engineering

Hengbin Zheng[1], Wenjun Dai[2], Zeyu Wang*[3] and Adham E. Ragab[4]

[1]*College of Water Conservancy and Civil Engineering, South China Agricultural University, Guangzhou, Guangdong, 510642, China*
[2]*Shenzhen Urban Transport Planning Center Co., Ltd, Shenzhen 518000, China*
[3]*School of Engineering and Technology, China University of Geosciences, Beijing, 100083, China*
[4]*Industrial Engineering Department, College of Engineering, King Saud University, PO Box 800, Riyadh 11421, Saudi Arabia*

(*Received March 29, 2023, Revised October 16, 2023, Accepted November 16, 2023*)

Abstract. When the amplitude of the vibrations is equivalent to that clearance, the vibrations for small amplitudes will really be significantly nonlinear. Nonlinearities will not be significant for amplitudes that are rather modest. Finally, nonlinearities will become crucial once again for big amplitudes. Therefore, the concrete panel system may experience a big amplitude in this work as a result of the high temperature. Based on the 3D modeling of the shell theory, the current work shows the influences of the von Kármán strain-displacement kinematic nonlinearity on the constitutive laws of the structure. The system's governing Equations in the nonlinear form are solved using Kronecker and Hadamard products, the discretization of Equations on the space domain, and Duffing-type Equations. Thermo-elasticity Equations. are used to represent the system's temperature. The harmonic solution technique for the displacement domain and the multiple-scale approach for the time domain are both covered in the section on solution procedures for solving nonlinear Equations. An effective data-driven solution is often utilized to predict how different systems would behave. The number of hidden layers and the learning rate are two hyperparameters for the network that are often chosen manually when required. Additionally, the data-driven method is offered for addressing the nonlinear vibration issue in order to reduce the computing cost of the current study. The conclusions of the present study may be validated by contrasting them with those of data-driven solutions and other published articles. The findings show that certain physical and geometrical characteristics have a significant effect on the existing concrete panel structure's susceptibility to temperature change and GPL weight fraction. For building construction industries, several useful recommendations for improving the thermo-mechanics' behavior of structural concrete panels are presented.
Keywords: efficient data-driven solution; nanocomposites; nonlinearities; thermo-elasticity; 3D-shell

1. Introduction

Carbon atoms are organized in a hexagonal lattice on a two-dimensional nanoscale to form graphene nanosheets (GPLs). There is now a great deal of interest in employing LPG and its derivatives for numerous applications, including gas sensing, tuning of electrical characteristics (Gaj *et al*. 2020), chemical and biological applications (Fei *et al*. 2020), solar cells, and photovoltaics (Cui *et al*. 2021), due to the unique nanostructure and distinctive features of LPG. By giving polymer composites extra qualities and enhancing mechanical stiffness, GPL and its derivatives seem to be excellent prospects to revolutionize the plastics industry in structural engineering (Wang *et al*. 2021). As low as 0.1 weight percent of LPG added to the polymer matrix has been shown to increase the strength of composites reinforced with 1.0 weight percent carbon nanotubes (CNT) (Rafiee *et al*. 2009). New composites reinforced with minimal GPL content, as opposed to traditional composites reinforced with high numbers of reinforcing fibers, have fewer issues with GPL adherence and deboning to the polymer matrix. These materials maintain the advantageous characteristics of polymers, such as high plastic deformation, durability, and excellent chemical and biological compatibility (Stankovich *et al*. 2006), while also increasing the hardness and durability of the material. This kind of materials can be used in fabrication of advanced structures (Alazwari *et al*. 2022a, b, Azandariani *et al*. 2022, Devnath *et al*. 2022, Kasiri and Massah 2022).

There have been several investigations on composites constructed of laminates and sandwich panels' dynamic behavior under heat stress. In order to explore the thermoelastic behavior of multilayer composites, Zhen *et al*. (2010) proposed an efficient higher-order model in which it was presupposed that thermal expansion had an impact on lateral displacement. Matsunaga (2007) suggested a higher-order 2D deformation theory to address the stability and free vibration of composites with corner-layer plates after enlarging the power chain displacement components. In the instance of the nonlinear behavior of a functionally graded (FG) beam under uniform thermal loading of the planner, Ma and Lee 2012 found an accurate solution. Using higher-order sandwich panel theory, Frostig and Thomsen (2009) concentrated on the impact of increasing temperatures on the free vibration of sandwich panels. With an emphasis on

*Corresponding author, Ph.D.,
E-mail: zeyu_wang@cugb.edu.cn

ISSN: 2287-237X (Print), 2287-2388 (Online)

composite panels, Kulikov and Plotnikova (2015) employed a surface sampling technique for a 3D steady-state thermo-elastic issue under heat stress. Khalili and Mohammadi (2012) modified higher-order theory involving sandwich panels was utilized to investigate the free vibration of heat-resistant sandwich panels with functionally categorized face panels. by splitting the horizontal displacement into the thickness of the stretched sections and the bending-shear deformation A novel higher-order theory was created by Houari *et al*. (2013) and utilized to examine the thermo-elastic bending of FG sandwich panels. The free vibrations of a sandwich panel that was exposed to thermal stress were the focus of Fazzolari and Carrera (2013). Liu *et al*. (2015) examined the random failure behavior of composite panels exposed to thermal buckling using the single-mode Fokker-Planck distribution. The FE formulation was created by Pandey and Pradyumna 2015) to examine heat-resistant FG sandwich panels. Additionally, several studies (Yang *et al*. 2022a, Zhang *et al*. 2023) have shown the significance of the solution technique in predicting the mechanical characteristics of diverse systems. Li *et al*. (2021) have examined the nonlinear vibrations and stability of double-curved laminated panels in thermal conditions in the area of linear/nonlinear vibration of double curved plates. Using a size-dependent nonlinear FE approach, Bidzard *et al*. (2022) investigated the free vibration of thermally loaded GPLRC multilayer microplates. In Ref. (Sahmani and Safaei 2021), the nonlinear stability behavior of microplates under axial compression was given as being microstructure-dependent and incorporating mobile mesh-free Kriging formulations, a third-order shear flexible shell model, and continuous gradient mechanics of changed deformation.

Artificial neural networks (ANN) and machine learning techniques are often used to forecast the behavior of scientific and technical systems (Li *et al*. 2023). Using the synthesis conditions of the chemical process, Moradi *et al*. (2022) employed machine learning regression to estimate particle size at the nanoscale. They came to the conclusion that precise and trustworthy findings may be attained by employing machine learning techniques. Neural networks may be quite successful in predicting the strength of concrete structures, according to Wang *et al*. (2021). Guo *et al*. (2022) employed fully connected NNs to analyze the frequency response of vibrating multilayer nanodiscs in the area of vibration. The quadrature differential technique and Hamilton's principle were used to derive and solve the governing Equations. The findings of the study suggest that ANN may be utilized to accurately anticipate the vibration of complicated structures. ANN was utilized by Babaei *et al*. (2022) to forecast beam oscillation behavior. According to studies in the fields of structural mechanics and ANNs, intensive computational effort in the fields of continuum mechanics and structural mechanics may be efficiently replaced by ANNs (Amelirad and Assempour 2019). Machine learning algorithm can be used in prediction of mechanical behavior of various complex systems (Guo *et al*. 2021, Ming *et al*. 2021, Wang and Zhang 2021, Zhou *et al*. 2022).

Researchers have discovered that stability analysis plays a significant role in supporting the mechanical response of systems (Feng *et al*. 2023, Safaei *et al*. 2023). In order to address this problem, Safaei (2021) introduced frequency-dependent damped vibrations of multifunctional foam plates sandwiched and integrated by composite faces. Yang *et al*. (2021) investigated the linear and nonlinear flexural responses of functionally graded composite microplates with changing thickness using an isogeometric couple stress continuum. Isogeometric analysis was used in Ref. (Wang *et al*. 2021) to examine the surface stress size dependence in nonlinear free oscillations of FGM quasi-3D nanoplates with arbitrary forms and variable thickness. Sobhani (2023a) looked at simulations of the vibrational characteristics of joining two separate semi-spheroidal shells and a full-spheroidal shell with a conical shell that is classified as undersea structures. Machine learning applications in additive manufacturing, from design through production and property control, were reviewed in Ref. (Sarkon *et al*. 2022). Graphene Oxide Powders (GOPs) were employed as a nano-reinforcement in a matrix to improve the vibrational properties of multifunctional structures (plate and shells) used in aerospace components, according to research by Sobhani (2023b). Ref. (İnada *et al*. 2022) performed a cutting-edge evaluation of the effectiveness of nanomaterials for solar energy storage devices. In Ref. (Rao *et al*. 2021), the porous FG composite microplates' isogeometric nonlinear bending analysis with a central cutout was represented using the pair stress continuum quasi-3D plate theory. Fan *et al*. (2021) investigated pair stress-based dynamic stability analysis for functionally graded composite truncated conical microshells with magnetostrictive face-sheets integrated within nonlinear viscoelastic foundations.

In order to produce computer hardware and software, computer engineering is a discipline of computer science and electronic engineering that combines several computer science and electronic engineering fields (Wang *et al*. 2022, Xu *et al*. 2022). Some colleges refer to computer engineering as computer science and engineering (Liu *et al*. 2021, Han *et al*. 2023). Training in electronic engineering, software engineering, computer science, software design, and hardware-software integration is necessary for computer engineers. It can include topics like computer networks, artificial intelligence, computer networks, robotics, computer architecture, and operating systems and applies the methods and concepts of electrical engineering and computer science (Tian *et al*. 2023, Yao *et al*. 2023). Computer engineers develop circuits as well as individual microcontrollers, microprocessors, personal computers, and supercomputers, among other hardware and software components of computing (He *et al*. 2023, Ren *et al*. 2023a). This branch of engineering focuses on both the internal workings of computer systems and their integration with broader systems (Zhou *et al*. 2021, Wu *et al*. 2023). Among the uses of computer engineering is robotics (Wang *et al*. 2022a, b) Writing firmware and software for embedded microcontrollers, designing chips, creating mixed signal circuit boards, creating analog sensors, and creating operating systems are among the topics typically covered by computer engineers (Shi *et al*. 2023, Shu *et al*. 2023). Robotics research, which primarily uses digital systems to

operate and monitor electrical systems including motors, communications, and sensors, is a good fit for computer engineers (Xue-feng *et al*. 2013, Dai *et al*. 2023). Since an undergraduate degree cannot encompass the entire range of knowledge required in the design and implementation of computers, many higher education institutions permit junior and senior computer engineering students to select areas of in-depth study (Huang *et al*. 2021, Sun *et al*. 2023). Before identifying computer engineering as their primary concentration, engineering students at other universities would be required to take one or two years of general engineering coursework (Wu *et al*. 2022, Yuan *et al*. 2023).

Some colleges refer to computer engineering as computer science and engineering (Zhou *et al*. 2023a). A bachelor's degree in computer science, electrical engineering, or computer engineering is typically required for entry-level computer engineering positions (Tang *et al*. 2023, Zhou *et al*. 2023b). A variety of mathematics, including calculus, algebra, and trigonometry, as well as some computer science classes, are typically required to be learned (Chen *et al*. 2023, Ren *et al*. 2023b). Because the domains of electronic and electric engineering are comparable, degrees in those fields are also acceptable (Kuang *et al*. 2018, Zhou *et al*. 2023c). Hardware engineers commonly work with computer software systems, so they need to have a strong foundation in computer programming (Lu *et al*. 2020, Hao *et al*. 2022). According to the Bureau of Labor Statistics (Lu *et al*. 2017, Lin *et al*. 2023), a computer engineering major is similar to an electrical engineering major with the addition of some computer science courses to the curriculum. Certain large organizations or specialized roles demand a master's degree (Yang *et al*. 2018a, Liu *et al*. 2020).

Computer engineers should also stay abreast of the swift advancements in technology (Yang *et al*. 2020, 2023). Consequently, a lot of people keep learning throughout their careers (Chen *et al*. 2021, Yang *et al*. 2022b). This can be beneficial, particularly in terms of picking up new abilities or honing ones that you already have (Yang *et al*. 2014, 2018b). For instance, there may be larger cost savings associated with producing and testing quality code as early in the process as feasible, especially prior to release, since the relative cost of correcting a fault rises the further along it is in the software development cycle (Hu *et al*. 2023, Wu *et al*. 2023). Because computer engineering creates more dependable, secure, and efficient computer hardware and software, it affects students' academic performance (Han *et al*. 2023a, b). Virtual reality and online learning, two recent developments in computer engineering, have revolutionized education by giving students flexible learning options and immersive experiences (Liu *et al*. 2021, Taheri *et al*. 2021). Computer engineering is a dynamic profession that has the ability to further transform education because it involves a variety of topics, such as electrical engineering concepts, hardware and software design, and working with software engineers (Taheri *et al*. 2020, Feng *et al*. 2021). The majority of computer engineers work for larger product development companies, and they might not need a license for this type of work (Firouzianhaji *et al*. 2021, Mehrabi *et al*. 2021). Independent consultants who promote computer engineering, like any other type of engineering (Toghroli *et al*. 2020), could be vulnerable to state regulations that limit the practice of professional engineering to individuals holding the relevant license (Taheri *et al*. 2019, Mehrabi *et al*. 2021).

The nonlinear thermo-elasticity performance of the concrete curved panels has not been studied, as can be observed from the previous papers. Based on the 3D modeling of the shell theory, the current work shows the influences of the von Kármán strain-displacement kinematic nonlinearity on the constitutive laws of the structure. The system's governing equations in the nonlinear form are solved using Kronecker and Hadamard products, the discretization of equations on the space domain, and Duffing-type equations. The system's temperature is represented using thermo-elasticity equations. The harmonic solution technique for the displacement domain and the multiple-scale approach for the time domain are both covered in the section on solution procedures for solving nonlinear Equations. An effective data-driven solution is often utilized to predict how different systems would behave. The number of hidden layers and the learning rate are two hyperparameters for the network that are often chosen manually when required. Additionally, the data-driven method is offered for addressing the nonlinear vibration issue in order to reduce the computing cost of the current study. The innovations in this book may be divided into the following four categories: 1. Presenting nonlinear thermoelastic equation. for a concrete panel with two curvatures. 2. Taking into account higher linear and nonlinear Winkler Pasternak terms to represent a real-world scenario. 3. Outlining a data-driven approach to estimating how the existing system would react in further difficult situations using simulation predictions as the train outcomes. 4. Outlining some useful recommendations for further research into the thermo-mechanics of structural concrete panel behavior for associated businesses.

2. Problem formulation

As previously stated, the current work examines the coupled thermo-elasticity performance of a composite panel made of FG and GPLR that is placed in an elastic foundation, as shown in Fig. 1a. Three distinct models are employed to depict the distribution of GPL nanoparticles across the panel's thickness, as illustrated in the image. Using a modified version of the well-known Halpin-Tsai micromechanics, the necessary Young moduli of the composite would be determined. These would be as follows:

$$E(z) = -\frac{3}{8}\frac{1+\xi_L\eta_L V_{GPL}}{\eta_L V_{GPL}-1}\times E_M - \frac{5}{8}\frac{1+\xi_W\eta_W V_{GPL}}{\eta_W V_{GPL}-1}\times E_M \quad (1)$$

where $\xi_L = 2\frac{l_{GPL}}{t_{GPL}}$, $\xi_W = 2\frac{w_{GPL}}{t_{GPL}}$, $V^*_{GPL} = \frac{\Lambda_{GPL}}{\left(\frac{\rho_{GPL}}{\rho_M}\right)(1-\Lambda_{GPL})+\Lambda_{GPL}}$, $\eta_W = -\frac{1-\left(\frac{E_{GPL}}{E_M}\right)}{\xi_W+\left(\frac{E_{GPL}}{E_M}\right)}$, and $\eta_L = \frac{\left(\frac{E_{GPL}}{E_M}\right)-1}{\left(\frac{E_{GPL}}{E_M}\right)+\xi_L}$. The well-known rule

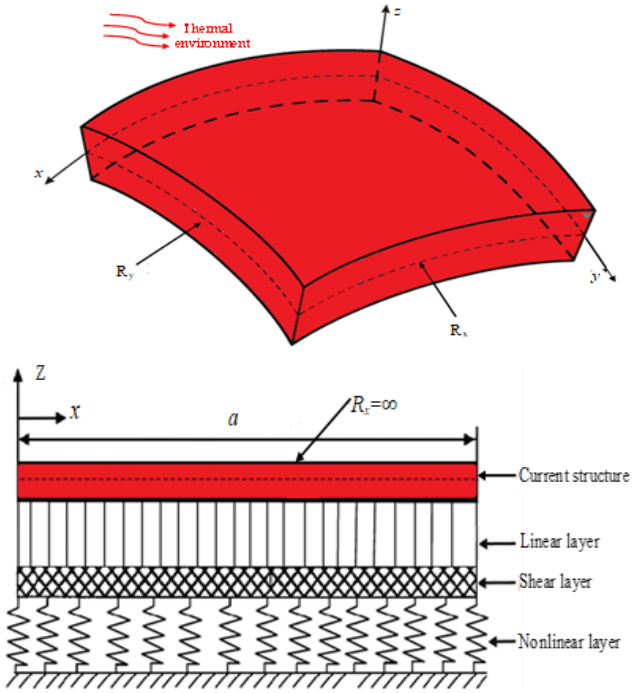

Fig. 1a GPLR composite panel geometrical measurements and a schematic inserted on a nonlinear elastic basis in a thermal environment

of mixtures (ROM), as shown below, would be used to determine the specific heat, Poisson's ratio, and mass density of the composite plate

$$\begin{aligned}\rho(z) &= \rho_{GPL}V_{GPL} + \rho_M(1 - V_{GPL}),\\ \nu(z) &= \nu_{GPL}V_{GPL} + \nu_M(1 - V_{GPL}),\\ \alpha(z) &= \alpha_{GPL}V_{GPL} + \alpha_M(1 - V_{GPL}),\\ C(z) &= C_{GPL}V_{GPL} + C_m(1 - V_{GPL}).\end{aligned} \tag{2}$$

The formula below is used to calculate the plate's shear modulus

$$G(z) = \frac{E(z)}{2(1+\nu(z))} \tag{3}$$

In this research, three different models of GPL distribution are taken into consideration and mathematically characterized as follows:

$$\begin{aligned}&GPL\text{-}O\text{: } V_{GPL} = 2V^*_{GPL}\left(1 - 2|\frac{z}{h}|\right)\\ &GPL\text{-}X\text{: } V_{GPL} = 4V^*_{GPL}|\frac{z}{h}|\\ &GPL\text{-}UD\text{: } V_{GPL} = V^*_{GPL}\end{aligned} \tag{4}$$

where $z = \frac{(k-1)h}{N_L-1} - \frac{h}{2},\ k = 1, \dots, N_L.$

Additionally, K_c, the associated thermal conductivity, would be calculated as follows for each distribution of GPL:

$$\text{GPL} - \text{UD: } \frac{K_c}{k_m} = 1 + D \tag{5a}$$

$$\text{GPL-X: } \frac{K_c}{k_m} = 1 + 4D|\frac{z}{h}| \tag{5b}$$

$$\text{GPL-O: } \frac{K_c}{k_m} = 1 + 2D\left(1 - 2|\frac{z}{h}|\right) \tag{5c}$$

where

$$D = \frac{1}{3}V^*_{GPL}\left\{\frac{2}{H + \frac{1}{\frac{K_x}{k_m}-1}} + \frac{1}{\frac{1}{2}(1-H) + \frac{1}{\frac{K_z}{k_m}-1}}\right\} \tag{61}$$

$$H = \frac{Ln\left[\varphi\left(\varphi + \sqrt{\varphi^2 - 1}\right)\right]}{\sqrt{(\varphi^2-1)^3}} - \frac{1}{\varphi^2 - 1} \tag{6b}$$

$$K_x = \frac{k_{GPL}}{\frac{2R_k k_{GPL}}{l_{GPL}} + 1} \tag{6c}$$

$$K_z = \frac{k_{GPL}}{\frac{2R_k k_{GPL}}{t_{GPL}} + 1} \tag{6d}$$

$$\varphi = \frac{l_{GPL}}{t_{GPL}} \tag{6e}$$

Additionally, the usual strain varies nonlinearly with thickness. resulting in an open, curved shell:

$$\begin{aligned}u(x,y,z,t) &= A_x u_0(x,y,t) - z\frac{\partial w(x,y,t)}{\partial x} +\\ &f(z)(\frac{\partial w(x,y,t)}{\partial x} + u_1(x,y,t)),\\ v(x,y,z,t) &= A_y v_0(x,y,t) - z\frac{\partial w(x,y,t)}{\partial y} +\\ &f(z)(\frac{\partial w(x,y,t)}{\partial y} + v_1(x,y,t)),\\ w(x,y,z,t) &= w_0(x,y,t).\end{aligned} \tag{7}$$

In Eq. (4), A_x and A_y are equal to $(1 + \frac{z}{R_x})$, and $(1 + \frac{z}{R_y})$, respectively. Eq. (8)'s in-plane displacement parameters are w_0, v_0, and u_0. Additionally, (x, y) shifts a random point (x, y) towards the center of the shell. Additionally, the y- and x-axes of v_1 and u_1 are each spinning. Below, in Eq. (5), the structural strain-stress Equation is shown:

$$\begin{aligned}\sigma_{xx} &= Q_{11}(\varepsilon_{xx} - \alpha_c\Delta T) + Q_{12}(\varepsilon_{yy} - \alpha_c\Delta T),\\ \sigma_{yy} &= Q_{12}(\varepsilon_{xx} - \alpha_c\Delta T) + Q_{22}(\varepsilon_{yy} - \alpha_c\Delta T),\\ \tau_{yz} &= Q_{44}\gamma_{yz},\ \tau_{xz} = Q_{55}\gamma_{xz},\ \tau_{xy} = Q_{55}\gamma_{xy}.\end{aligned} \tag{8}$$

$$\begin{aligned}Q_{11} = Q_{22} &= \frac{E}{(1-\nu)^2},\ Q_{12} = \frac{\nu E}{(1-\nu)^2}\\ Q_{44} = Q_{55} = Q_{66} &= \frac{E}{2(1+\nu)}.\end{aligned}$$

By assuming without heat generation in the system and steady state:

$$\frac{1}{A_xA_y}\left[\frac{\partial}{\partial x}\left(\mathrm{K}_c\frac{\partial(\mathrm{T}-T_0)}{\partial\alpha}\frac{A_y}{A_x}\right)+\frac{\partial}{\partial y}\left(\mathrm{K}_c\frac{\partial(\mathrm{T}-T_0)}{\partial\beta}\frac{A_x}{A_y}\right)+\frac{\partial}{\partial z}\left(\mathrm{K}_c\frac{\partial(\mathrm{T}-T_0)}{\partial z}A_xA_y\right)\right]=0 \tag{9}$$

Thermal surface boundary conditions are:

$$\begin{aligned}T(0,y,z)=T_0, T(a,y,z)=T_0, T(x,0,z)\\ =T_0, T(x,b,z)=T_0, T(x,y,-h/2)\\ =T_0, T(x,y,h/2)=T\end{aligned} \tag{10}$$

where T_0 represent the ambient temperature. In addition to, (σ_{xx}, σ_{yy}, τ_{yz}, τ_{xz}, τ_{xy}) are the stresses and (ε_{xx}, ε_{yy}, γ_{yz}, γ_{xz}, γ_{xy}) is strains in linear form. The *z*, *x*, and *y* axes' respective elastic coefficients are known as Q_{ij}. As a consequence, it is possible to express the following correlations between strain and displacement:

$$\begin{aligned}\varepsilon_{xx}&=\frac{1}{A_x}\left(\frac{\partial u}{\partial x}+\frac{w}{R_x}+\frac{1}{2}\left(\frac{\partial w}{\partial x}\right)^2\right),\\ \varepsilon_{yy}&=\frac{1}{A_y}\left(\frac{\partial v}{\partial y}+\frac{w}{R_y}+\frac{1}{2}\left(\frac{\partial w}{\partial y}\right)^2\right),\\ \gamma_{xz}&=\frac{1}{A_x}\left(\frac{\partial w}{\partial x}-\frac{u}{R_x}\right)+\frac{\partial u}{\partial z},\\ \gamma_{yz}&=\frac{\partial v}{\partial z}+\frac{1}{A_y}\left(\frac{\partial w}{\partial y}-\frac{v}{R_y}\right),\\ \gamma_{xy}&=\frac{1}{A_x}\frac{\partial v}{\partial x}+\frac{1}{A_y}\frac{\partial u}{\partial y}+\frac{1}{A_xA_y}\frac{\partial w}{\partial x}\frac{\partial w}{\partial y}\end{aligned} \tag{11}$$

Using the variational energy method, the motion equations. and related boundary conditions (B. Cs) of the shell may be specified:

$$\int_{t_1}^{t_2}(\delta\mathcal{T}-\delta\mathcal{U}-\delta\mathcal{W})dt=0 \tag{12}$$

where kinetic energy is [108]:

$$\delta\mathcal{T}=\iiint_V\rho\left(\frac{\partial u}{\partial t}\frac{\partial\delta u}{\partial t}+\frac{\partial v}{\partial t}\frac{\partial\delta v}{\partial t}+\frac{\partial w}{\partial t}\frac{\partial\delta w}{\partial t}\right)dV \tag{13}$$

The strain energy for open-type shells may also be expressed using the following Equation.

$$\delta\mathcal{U}=\int_{-\mathrm{h}/2}^{\mathrm{h}/2}\iint_{\mathrm{A}}\left(\sigma_{\mathrm{xx}}\delta\varepsilon_{\mathrm{xx}}+\sigma_{\mathrm{yy}}\delta\varepsilon_{\mathrm{yy}}+\tau_{\mathrm{yz}}\delta\gamma_{\mathrm{yz}}+\tau_{\mathrm{xz}}\delta\gamma_{\mathrm{xz}}+\tau_{\mathrm{xy}}\delta\gamma_{\mathrm{xy}}\right)\mathrm{dV} \tag{14}$$

The strain energy resulting from a nonlinear elastic basis may also be expressed as

$$\delta\mathcal{W}=\int_A\{K_1w_0\delta w_0+K_3w_0^3\delta w_0+K_4w_0^5\delta w_0-K_2\left[\frac{\partial^2w_0}{\partial x^2}+\frac{\partial^2w_0}{\partial y^2}\right]\delta w_0\}\,dA \tag{15}$$

The linear Winkler foundation, linear Pasternak foundation, and nonlinear Winkler foundation are, respectively, their parameters are defined by $K_1\left(\frac{N}{m^3}\right)$, $K_2\left(\frac{N}{m}\right)$, $K_3\left(\frac{N}{m^5}\right)$, and $K_4\left(\frac{N}{m^7}\right)$. Finally, substituting Eqs. (13)-(15) in Eq. (12), motion equations of the current system are acquired as:

$$\delta u_0:\frac{\partial N_{xx}}{\partial x}+\frac{N_{xz}}{R_x}-R_{xz}+\frac{\partial Q_{xy}}{\partial y}=I_0^{u_0}\frac{\partial^2u_0}{\partial t^2}-I_1^{u_0}\frac{\partial^3w_0}{\partial x\partial t^2}+I_2^{u_0}\frac{\partial^3w_0}{\partial x\partial t^2}+I_2^{u_0}\frac{\partial^2u_1}{\partial t^2}, \tag{16a}$$

$$\delta v_0:\frac{\partial N_{yy}}{\partial y}+\frac{N_{yz}}{R_y}-R_{yz}+\frac{\partial N_{xy}}{\partial x}=I_0^{v_0}\frac{\partial^2v_0}{\partial t^2}-I_1^{v_0}\frac{\partial^3w_0}{\partial y\partial t^2}+I_2^{v_0}\frac{\partial^3w_0}{\partial y\partial t^2}+I_2^{v_0}\frac{\partial^2v_1}{\partial t^2}, \tag{16b}$$

$$\begin{aligned}\delta w_0:&\frac{\partial^2P_{xx}}{\partial x^2}-\frac{\partial^2Q_{xx}}{\partial x^2}-\frac{M_{xx}}{R_x}+\frac{\partial}{\partial x}\left(M_{xx}\frac{\partial w_0}{\partial x}\right)+\frac{\partial^2P_{yy}}{\partial y^2}-\frac{\partial^2Q_{yy}}{\partial y^2}-\frac{M_{yy}}{R_y}+\frac{\partial}{\partial y}\left(M_{yy}\frac{\partial w_0}{\partial y}\right)+\frac{\partial M_{yz}}{\partial y}+\frac{1}{R_y}\frac{\partial P_{yz}}{\partial y}-\frac{1}{R_y}\frac{\partial Q_{yz}}{\partial y}-\frac{\partial N_{yz}}{\partial y}+\frac{\partial S_{yz}}{\partial y}+\frac{\partial M_{xz}}{\partial x}+\frac{1}{R_x}\frac{\partial P_{xz}}{\partial x}-\frac{1}{R_x}\frac{\partial Q_{xz}}{\partial x}-\frac{\partial N_{xz}}{\partial x}+\frac{\partial S_{xz}}{\partial x}+\frac{\partial^2M_{xy}}{\partial x\partial y}-\frac{\partial^2P_{xy}}{\partial x\partial y}+\frac{\partial^2R_{xy}}{\partial x\partial y}-\frac{\partial^2S_{xy}}{\partial x\partial y}+\frac{1}{2}\frac{\partial}{\partial x}\left(T_{xx}\frac{\partial w_0}{\partial y}\right)+\frac{1}{2}\frac{\partial}{\partial y}\left(T_{xx}\frac{\partial w_0}{\partial x}\right)-K_1w_0-K_3w_0^3-K_4w_0^5+K_2\left[\frac{\partial^2w_0}{\partial x^2}+\frac{\partial^2w_0}{\partial y^2}\right]-N^T\nabla^2w_0=I_0^{w_0}\frac{\partial^2w_0}{\partial t^2}-\left(I_3^{u_0}\frac{\partial^3u_0}{\partial x\partial t^2}-I_4^{u_0}\frac{\partial^4w_0}{\partial x^2\partial t^2}+I_5^{u_0}\frac{\partial^4w_0}{\partial x^2\partial t^2}+I_5^{u_0}\frac{\partial^3u_1}{\partial x\partial t^2}\right)+\left(I_6^{u_0}\frac{\partial^3u_0}{\partial x\partial t^2}-I_7^{u_0}\frac{\partial^4w_0}{\partial x^2\partial t^2}+I_8^{u_0}\frac{\partial^4w_0}{\partial x^2\partial t^2}+I_8^{u_0}\frac{\partial^3u_1}{\partial x\partial t^2}\right)-\left(I_3^{v_0}\frac{\partial^3v_0}{\partial y\partial t^2}-I_4^{v_0}\frac{\partial^4w_0}{\partial y^2\partial t^2}+I_5^{v_0}\frac{\partial^4w_0}{\partial y^2\partial t^2}+I_5^{v_0}\frac{\partial^3v_1}{\partial y\partial t^2}\right)+\left(I_6^{v_0}\frac{\partial^3v_0}{\partial y\partial t^2}-I_7^{v_0}\frac{\partial^4w_0}{\partial y^2\partial t^2}+I_8^{v_0}\frac{\partial^4w_0}{\partial y^2\partial t^2}+I_8^{v_0}\frac{\partial^3v_1}{\partial y\partial t^2}\right),\end{aligned} \tag{16c}$$

$$\delta u_1:\frac{\partial Q_{xx}}{\partial x}+\frac{Q_{xz}}{R_x}-S_{xz}+\frac{\partial S_{xy}}{\partial y}=I_0^{u_1}\frac{\partial^2u_0}{\partial t^2}-I_1^{u_1}\frac{\partial^3w_0}{\partial x\partial t^2}+I_2^{u_1}\frac{\partial^3w_0}{\partial x\partial t^2}+I_2^{u_1}\frac{\partial^2u_1}{\partial t^2}, \tag{16d}$$

$$\delta v_1:\frac{\partial Q_{yy}}{\partial y}+\frac{Q_{yz}}{R_y}-S_{yz}+\frac{\partial P_{xy}}{\partial y}=I_0^{v_1}\frac{\partial^2v_0}{\partial t^2}-I_1^{v_1}\frac{\partial^3w_0}{\partial y\partial t^2}+I_2^{v_1}\frac{\partial^3w_0}{\partial y\partial t^2}+I_2^{v_1}\frac{\partial^2v_1}{\partial t^2}. \tag{16e}$$

In which:

$$\begin{aligned}\{N_{xx},M_{xx},P_{xx},Q_{xx}\}&=\int_V\frac{1}{A_x}\{A_x,1,z,f(z)\}\sigma_{xx}dV,\\ \{N_{yy},M_{yy},P_{yy},Q_{yy}\}&=\int_V\frac{1}{A_y}\{A_y,1,z,f(z)\}\sigma_{yy}dV,\\ \{N_{xz},M_{xz},P_{xz},Q_{xz},R_{xz},S_{xz}\}&=\int_V\left\{1,\frac{1}{A_x},\frac{z}{A_x},\frac{f(z)}{A_x},\frac{\partial A_x}{\partial z},f'(z)\right\}\tau_{xz}dV,\\ \{N_{yz},M_{yz},P_{yz},Q_{yz},R_{yz},S_{yz}\}&=\int_V\left\{1,\frac{1}{A_y},\frac{z}{A_y},\frac{f(z)}{A_y},\frac{\partial A_y}{\partial z},f'(z)\right\}\tau_{yz}dV,\\ \{N_{xy},M_{xy},P_{xy},Q_{xy},R_{xy},S_{xy},T_{xy}\}&=\int_V\left\{\frac{A_y}{A_x},\frac{z}{A_x},\frac{f(z)}{A_x},\frac{A_x}{A_y},\frac{z}{A_y},\frac{f(z)}{A_y},\frac{1}{A_xA_y}\right\}\tau_{xy}dV,\\ N^T&=\int_V\{Q_{11}+Q_{12}+Q_{13}\}\alpha_c\Delta TdV,\\ \{I_0^{u_0},I_1^{u_0},I_2^{u_0}\}&=\int_V A_x\rho\{A_x,z,f(z)\}\,dV,\end{aligned} \tag{17}$$

$$\{I_0^{w_0}\} = \int_V \rho\, dV,$$

$$\{I_3^{u_0}, I_4^{u_0}, I_5^{u_0}\} = \int_V z\rho\{A_x, z, f(z)\}\, dV,$$

$$\{I_6^{u_0}, I_7^{u_0}, I_8^{u_0}\} = \int_V f(z)\rho\{A_x, z, f(z)\}\, dV,$$

$$\{I_0^{u_1}, I_1^{u_1}, I_2^{u_1}\} = \int_V f(z)\rho\{A_x, z, f(z)\}\, dV,$$

$$\{I_0^{v_0}, I_1^{v_0}, I_2^{v_0}\} = \int_V A_y\rho\{A_y, z, f(z)\}\, dV,$$

$$\{I_3^{v_0}, I_4^{v_0}, I_5^{v_0}\} = \int_V z\rho\{A_y, z, f(z)\}\, dV,$$

$$\{I_6^{v_0}, I_7^{v_0}, I_8^{v_0}\} = \int_V f(z)\rho\{A_y, z, f(z)\}\, dV,$$

$$\{I_0^{v_1}, I_1^{v_1}, I_2^{v_1}\} = \int_V f(z)\rho\{A_y, z, f(z)\}\, dV,$$

The following are the present microstructure's boundary conditions:

$$\delta u_0\colon (N_{xx})\hat{n}_x + (Q_{xy})\hat{n}_y = 0,$$

$$\delta v_0\colon (N_{xy})\hat{n}_x + (N_{yy})\hat{n}_y = 0,$$

$$\begin{aligned}\delta w_0\colon &\left(-\frac{\partial P_{xx}}{\partial x} - M_{xx}\frac{\partial w_0}{\partial x} + M_{xz} + \frac{P_{xz}}{R_x} - \frac{Q_{xz}}{R_x} - N_{xz} + S_{xz} + \frac{1}{2}\frac{\partial M_{xy}}{\partial y} - \frac{1}{2}\frac{\partial P_{xy}}{\partial y} + \frac{1}{2}\frac{\partial R_{xy}}{\partial y} - \frac{1}{2}\frac{\partial S_{xy}}{\partial y} + \frac{1}{2}T_{xx}\frac{\partial w_0}{\partial y}\right)\hat{n}_x + \\ &\left(-\frac{\partial P_{yy}}{\partial y} - M_{yy}\frac{\partial w_0}{\partial y} + M_{yz} + \frac{P_{yz}}{R_y} - \frac{Q_{yz}}{R_y} - N_{yz} + S_{yz} + \frac{1}{2}\frac{\partial M_{xy}}{\partial x} - \frac{1}{2}\frac{\partial P_{xy}}{\partial x} + \frac{1}{2}\frac{\partial R_{xy}}{\partial x} - \frac{1}{2}\frac{\partial S_{xy}}{\partial x} + \frac{1}{2}T_{xx}\frac{\partial w_0}{\partial x}\right)\hat{n}_y = 0,\end{aligned} \tag{18}$$

$$\delta u_1\colon (Q_{xx})\hat{n}_x + (S_{xy})\hat{n}_y = 0,$$

$$\delta v_1\colon (S_{xy})\hat{n}_x + (Q_{yy})\hat{n}_y = 0.$$

3. Solution procedure

3.1 Discretization in space domain

The equations of motion and related BCs were discretized using GDQ for this inquiry. A variable function $f(x)$ may be written across the interval $[x_1, \ldots, x_n]$, and its rth-order derivative at x_i is

$$\frac{d^r f(x)}{dx^r} = \sum_{j=1}^{N} D_{ij}^{(r)} f(x_j) \tag{19}$$

and the recursion formula displays the weighting factors for the rth-order derivative $D_{ij}^{(r)}$

$$D_{ij}^{(r)} = \begin{cases} I_{ij} & r = 0 \\ \dfrac{\wp(x_i)}{(x_i - x_j)\wp(x_j)} & i,j = 1, \ldots, N \text{ and } i \neq j \text{ and } r = 1 \\ r\left[W_{ij}^{(1)} W_{ii}^{(r-1)} - \dfrac{W_{ij}^{(r-1)}}{x_i - x_j}\right], & i \neq j \\ -\sum\limits_{\substack{k=1 \\ k\neq i}}^{N} W_{ik}^{(r)}, & i = j \end{cases} \quad i,j = 1, \ldots, N \text{ and } r \geqslant 2 \tag{20}$$

In which identity matrix is shown by I_{ij} and $\wp(x_i)$ can be described by $\prod_{k=1,i\neq k}^{N}(x_i - x_k)$. The GDQ technique may be used to a 2-D system to anticipate partially derivatives of the function $f(x,y)$ defined on $[x_1, \ldots, x_n]$ and $[y_1, \ldots, y_m]$. This is done by using the Kronecker tensor product, which is represented as $\otimes$. The partial derivative of second-order for x and y would be

$$\frac{\partial^2 f(x,y)}{\partial x \partial y} = \left(\mathrm{D}_y^{(1)} \otimes \mathrm{D}_x^{(1)}\right)\bar{\mathrm{f}} \tag{21}$$

where $\bar{\mathrm{f}}$ can be written as

$$\bar{\mathrm{f}} = \begin{matrix}[f(x_1,y_1), \ldots, f(x_n,y_1), f(x_1,y_2), \ldots \\ f(x_n,y_2), \ldots, f(x_1,y_m), \ldots, f(x_n,y_m)]\end{matrix}^{\mathrm{T}} \tag{22}$$

in which N and M are the x, y coordinates of grid points, respectively. Consider the 2D functions $v_1(x,y)$, $u_1(x,y)$, $w_0(x,y)$, $v_0(x,y)$ and $u_0(x,y)$. Using the shifted Chebyshev-Gauss-Lobatto technique, one can determine the distribution of grid points along x and y

$$\begin{aligned} x_i &= \frac{1}{2}\left(1 - \cos\frac{i-1}{N-1}\pi\right), i = 1{:}N, \\ y_j &= \frac{1}{2}\left(1 - \cos\frac{j-1}{M-1}\pi\right), j = 1{:}M. \end{aligned} \tag{23}$$

By incorporating Eqs. (16) through (17), accounting for Eq. (19), and presenting them in a discretized form, the following may be expressed.

$$\mathrm{M}\ddot{\mathrm{X}} + \mathrm{KX} + \mathrm{K}_{nl}(\mathrm{X}) = 0 \tag{24}$$

Over-dotting in Eq. (24), which represents the field variables vector, stiffness matrix, mass matrix, and nonlinear stiffness vector, respectively, reveals derivatives relevant to.

$$\begin{aligned} \mathrm{X} &= [\bar{u}_0, \bar{v}_0, \bar{w}_0, \bar{u}_1, \bar{v}_1]^{\mathrm{T}}, \\ \mathrm{K}_{nl}(\mathrm{X}) &= [\mathrm{R}_1, \mathrm{R}_2, \mathrm{R}_3, \mathrm{R}_4, \mathrm{R}_5]^{\mathrm{T}}, \\ I &= \left[I_{ij}\right] \quad i,j = 1, \ldots, 5, \\ M &= \left[M_{ij}\right] \quad i,j = 1, \ldots, 5, \end{aligned} \tag{25}$$

where displacement variables column vector are $\bar{\mathrm{u}}_0$, $\bar{\mathrm{v}}_0$, $\bar{\mathrm{w}}_0$, $\bar{\mathrm{u}}_1$ and $\bar{\mathrm{v}}_1$ which can be expressed by Eq. (26)

$$\begin{aligned} \bar{\mathrm{u}}_0 &= \begin{matrix}[u_0(x_1,y_1), \ldots, u_0(x_n,y_1), u_0(x_1,y_2), \ldots \\ u_0(x_n,y_2), \ldots, u_0(x_1,y_m), \ldots, u_0(x_n,y_m)]\end{matrix}^{\mathrm{T}}, \\ \bar{\mathrm{v}}_0 &= \begin{matrix}[v_0(x_1,y_1), \ldots, v_0(x_n,y_1), \mathfrak{v}_i(x_1,y_2), \ldots \\ v_0(x_n,y_2), \ldots, v_0(x_1,y_m), \ldots, v_0(x_n,y_m)]\end{matrix}^{\mathrm{T}}, \\ \bar{\mathrm{w}}_0 &= \begin{matrix}[w_0(x_1,y_1), \ldots, w_0(x_n,y_1), w_0(x_1,y_2), \ldots \\ w_0(x_n,y_2), \ldots, w_0(x_1,y_m), \ldots, w_0(x_n,y_m)]\end{matrix}^{\mathrm{T}}, \\ \bar{\mathrm{u}}_1 &= \begin{matrix}[u_1(x_1,y_1), \ldots, u_1(x_n,y_1), u_1(x_1,y_2), \ldots \\ u_1(x_n,y_2), \ldots, u_1(x_1,y_m), \ldots, u_1(x_n,y_m)]\end{matrix}^{\mathrm{T}}, \\ \bar{\mathrm{v}}_1 &= \begin{matrix}[v_1(x_1,y_1), \ldots, v_1(x_n,y_1), v_1(x_1,y_2), \ldots \\ v_1(x_n,y_2), \ldots, v_1(x_1,y_m), \ldots, v_1(x_n,y_m)]\end{matrix}^{\mathrm{T}}, \end{aligned} \tag{26}$$

The symbol $\circ$ shows Hadamard product.

3.2 Finding Duffing-type Eqs.

In this subsection, the particle differential Eq. of motion' transformation to the Eqs. of Duffing-type ordinary is presented. It is possible to find an eigenvalue issue in its general form if a harmonic solution is presented as $\mathrm{X} = \widetilde{\mathrm{X}}e^{j\omega\tau}$. By substituting BCs for the stiffness and inertia matrices in Eq. (24) and eliminating the nonlinear components, it is possible to create a common form of an eigenvalue issue.

$$\begin{gathered}\mathrm{K}\widetilde{\mathrm{X}} = \omega^2\mathrm{M}\widetilde{\mathrm{X}},\\ \widetilde{\mathrm{X}} = [\tilde{u}_0^T, \tilde{v}_0^T, \tilde{w}_0^T, \tilde{u}_1^T, \tilde{v}_1^T]^{\mathrm{T}}.\end{gathered} \tag{27}$$

the linear frequencies and their mode forms as a result of solving Eq. (27) as below:

$$\mathrm{X} = \Phi\mathrm{q} \tag{28}$$

where sparse matrix and reduced generalized coordinates are represented by Φ and q, which are Galerkin basic functions of first m mode forms. You might define Φ and q using Eqs. (29) and (30) as follows:

$$\mathrm{q}^{\mathrm{T}}_{(2m)\times 1} = \begin{bmatrix} q_{u_0}^{(1)}, q_{u_0}^{(2)}, \dots, q_{u_0}^{(m)}, \\ q_{v_0}^{(1)}, q_{v_0}^{(2)}, \dots, q_{v_0}^{(m)} \\ q_{w_0}^{(1)}, q_{w_0}^{(2)}, \dots, q_{w_0}^{(m)}, \\ q_{u_1}^{(1)}, q_{u_1}^{(2)}, \dots, q_{u_1}^{(m)}, \\ q_{v_1}^{(1)}, q_{v_1}^{(2)}, \dots, q_{v_1}^{(m)} \end{bmatrix}, \tag{29}$$

$$\Phi = \begin{bmatrix} \Phi_{u_0} & 0 & 0 & 0 & 0 \\ 0 & \Phi_{v_0} & 0 & 0 & 0 \\ 0 & 0 & \Phi_{w_0} & 0 & 0 \\ 0 & 0 & 0 & \Phi_{u_1} & 0 \\ 0 & 0 & 0 & 0 & \Phi_{v_1} \end{bmatrix},$$

in which the components of Φ are

$$\begin{gathered}\Phi_{u_0} = \left[\left\{\chi_{u_0}^1\right\}_{N\times M}, \dots, \left\{\chi_{u_0}^m\right\}_{N\times M}\right],\\ \Phi_{v_0} = \left[\left\{\chi_{v_0}^1\right\}_{N\times M}, \dots, \left\{\chi_{v_0}^m\right\}_{N\times M}\right],\\ \Phi_{w_0} = \left[\left\{\chi_{w_0}^1\right\}_{N\times M}, \dots, \left\{\chi_{w_0}^m\right\}_{N\times M}\right].\\ \Phi_{u_1} = \left[\left\{\chi_{u_1}^1\right\}_{N\times M}, \dots, \left\{\chi_{u_1}^m\right\}_{N\times M}\right],\\ \Phi_{v_1} = \left[\left\{\chi_{v_1}^1\right\}_{N\times M}, \dots, \left\{\chi_{v_1}^m\right\}_{N\times M}\right],\end{gathered} \tag{30}$$

Substituting Eq. (28) into (24) gives the residuals

$$\mathrm{R} = \mathrm{M}\Phi\ddot{\mathrm{q}} + \mathrm{K}\Phi\mathrm{q} + \mathrm{K}_{nl}(\Phi\mathrm{q}) \tag{31}$$

matrix operator can be defined as

$$\mathrm{G}_{m\times 12NM} = \Phi^{\mathrm{T}} diag(\mathrm{S}), \mathrm{S} = [\mathrm{S}_\xi, \mathrm{S}_\xi, \mathrm{S}_\xi, \mathrm{S}_\xi, \mathrm{S}_\xi]_{1\times(5NM)} \tag{32}$$

Integration across the domain may then be done by multiplying the mode forms in the relevant Equation. In the appendix, the integral operator S_ξ is studied. The following is the outcome of multiplying Eq. (32) by Eq. (31) (residual vector):

$$\widetilde{\mathrm{M}}\ddot{\mathrm{q}} + \widetilde{\mathrm{K}}\mathrm{q} + \widetilde{\mathrm{K}}_{nl}(\mathrm{q}) = 0 \tag{33}$$

where

$$\widetilde{\mathrm{M}} = \mathrm{GM}\Phi,\ \widetilde{\mathrm{K}} = \mathrm{GK}\Phi,\ \widetilde{\mathrm{K}}_{nl}(\mathrm{q}) = \mathrm{GK}_{nl}(\Phi\mathrm{q}) \tag{34}$$

3.3 Time domain solution

The defining normalized parameters $\Omega = 2\pi/\mathrm{T}$ and $\tau^* = \tau/\mathrm{T}$ would simplify Eq. (33) into

$$\left(\frac{\Omega}{2\pi}\right)^2 \widetilde{\mathrm{M}}\ddot{\mathrm{q}} + \widetilde{\mathrm{K}}\mathrm{q} + \widetilde{\mathrm{K}}_{nl}(\mathrm{q}) = 0 \tag{35}$$

where, the $\ddot{\mathrm{q}}$ is differentiation related to τ^*. Over time domain, q can be discretized by:

$$\mathrm{Q}_{5m\times N_t} = \begin{bmatrix} \mathrm{q}_{u_0\ 1\times N_t}^{(1)}, \dots, \mathrm{q}_{u_0\ 1\times N_t}^{(m)}, \\ \mathrm{q}_{v_0\ 1\times N_t}^{(1)}, \dots, \mathrm{q}_{v_0\ 1\times N_t}^{(m)}, \\ \mathrm{q}_{w_0\ 1\times N_t}^{(1)}, \dots, \mathrm{q}_{w_0\ 1\times N_t}^{(m)}, \\ \mathrm{q}_{u_1\ 1\times N_t}^{(1)}, \dots, \mathrm{q}_{u_1\ 1\times N_t}^{(m)}, \\ \mathrm{q}_{v_1\ 1\times N_t}^{(1)}, \dots, \mathrm{q}_{v_1\ 1\times N_t}^{(m)}, \end{bmatrix} \tag{36}$$

where N_t is an even number of discretization points in the time domain and m is the number of Galerkin mode forms. At grid point τ_i^*, the value of $q(\tau_i^*)$ may be written as follows:

$$\tau_i^* = \frac{i}{N_t}, 0 < \tau_i \leqslant 1, i = 1,2,\dots,N_t = 2k \tag{37}$$

substituting Eq. (37) into (35) yields

$$\left(\frac{\Omega}{2\pi}\right)^2 \widetilde{\mathrm{M}}\mathrm{QD}_\tau^{(2)\mathrm{T}} + \widetilde{\mathrm{K}}\mathrm{Q} + \widetilde{\mathrm{K}}_{\mathrm{nl}}(\mathrm{Q}) = 0 \tag{38}$$

where the matrix of the time differentiation operator ($\mathrm{D}_\tau^{()}$) can be defined as follows:

$$\begin{gathered}\begin{cases} a_{11} = 0 \\ a_{i,1} = \frac{(-1)^{i-1}}{2}\cot\frac{\pi(i-1)}{\mathrm{n}_t} \\ a_{1,j} = \frac{(-1)^{N_t-j+1}}{2}\cot\frac{\pi(N_t-j+1)}{N_t} \\ a_{i+1,j+1} = a_{i,j} \end{cases}, \ i,j = 2,3,4,\dots,N_t,\\ \mathrm{D}_\tau^{(1)} = 2\pi[a_{i,j}],\end{gathered}$$

$$\begin{gathered}\begin{cases} b_{11} = -\frac{N_t^2}{12} - \frac{1}{6} \\ b_{i,1} = \frac{(-1)^{i-2}}{2\sin^2\frac{\pi(i-1)}{N_t}} \\ b_{1,j} = \frac{(-1)^{N_t-j}}{2\sin^2\frac{\pi(N_t-j+1)}{N_t}} \\ b_{i+1,j+1} = b_{i,j} \end{cases}, \quad i,j = 2,3,4,\dots,N_t,\\ \mathrm{D}_\tau^{(2)} = (2\pi)^2[b_{i,j}].\end{gathered} \tag{39}$$

In Eq. (39) the Teoplitz matrices are shown by $\mathrm{D}_\tau^{(2)}$ and $\mathrm{D}_\tau^{(1)}$. Eq. (38) can be vectorized as

$$\left(\left(\frac{\Omega}{2\pi}\right)^2 \left(\mathrm{D}_{\tau}^{(2)} \otimes \widetilde{\mathrm{M}}\right) + \left(\mathrm{I}_{\tau} \otimes \widetilde{\mathrm{K}}\right)\right) vec(\mathrm{Q}) + vec(\widetilde{\mathrm{K}}_{nl}(\mathrm{Q})) = 0 \quad (40)$$

Also, have:

$$\mathrm{H}: \mathbb{R}^{12m\times N_t+1} \rightarrow \mathbb{R}^{12m\times N_t}, \mathrm{H}(vec(\mathrm{Q}),\Omega) = 0 \quad (41)$$

Finally, the Eq. (40) can be solved via pseudo-arc-length continuation algorithm. For more detail please see Ref. (HB 1977).

4. Numerical findings and technical discussion

A list of GPLs reinforcement and concrete material are presented in Table 1. In this section, the verification, parameteric results, data-driven solution algorithm and the results of mentioned algorithm will be presented in detail.

4.1 Validation

To verify the results, the outcomes of the current work and Ref. are compared for dimensionless linear frequency and nonlinear to the linear frequency of the panel in Table 2. As is observed the comparison has been made for different temperature and CNT volume fraction. This table indicates that by increasing the CNT volume fraction, the dimensionless frequency increases while nonlinear to linear frequency has different behavior. For more detail, by increasing the CNT volume fraction, the frequency ratio (nonlinear to linear frequency) first decreases and then increases. So, the frequency ratio is sensitive to the value of the CNT volume fraction. By increasing the temperature, the dimensionless frequency decreases while the frequency ratio has different behavior. So, the nonlinear to linear frequency is very sensitive to the value of geometrical and physical parameters of the composite panel structure. The results show that the results are in good agreement with each other and the results of current work have been verified.

4.2 Data-Driven solution

The physics-based deep neural network developed in this study may be able to substitute the boundary value problem's finite element solution with the surface elasticity effect described above. The displacement field to the governing differential Eqs. can be solved directly by reducing the overall energy loss. Unlike basic approaches, the deep energy technique does not require the construction of explicit stiffness matrices for surface and bulk materials, nor does it require the lengthy discretization of meshes. maximum. Finite element techniques struggle to avoid deformed components while discretizing the mesh in a complex structure. Deep energy methods, on the other hand, may totally randomize concentration sites using Monte Carlo simulation. The primary benefit of this approach is that the displacement field, which is produced by the neural network, is indefinitely differentiable. Because of this, the

Table 1 The involved materials properties

Concrete (matrix)	GPL
$v_M = 0.2$	$v_{GPL} = 0.186$
$\rho_M\ (\frac{kg}{m^3}) = 2.3 \times 10^3$	$\rho_{GPL}(\frac{kg}{m^3}) = 1.06 \times 10^3$
$E_M\ (GPa) = 25$	$E_{GPL}\ (TPa) = 1.01$
$k_M\ (\frac{w}{mk}) = 1.8$	$k_{GPL}\ (\frac{w}{mk}) = 2000$
$\alpha_M\ (\frac{10^{-5}}{k}) = 0.1$	$\alpha_{GPL}\ (\frac{10^{-5}}{k}) = 2.35$
$C_M\ (\frac{J}{kg\ k}) = 880$	$C_{GPL}\ (\frac{J}{kg\ k}) = 8.03 \times 10^7$
	$R_k(\frac{m^2k}{w}) = 10^{-8}$
	$l_{GPL}(\mu m) = 2.5$
	$w_{GPL}(\mu m) = 1.5$
	$t_{GPL}(nm) = 1.5$

Table 2 Comparison of linear frequency and nonlinear to linear frequency of panel with $a/b = 1$, $\frac{a}{R_x} = 1$, $\frac{b}{h} = 20$, $h = 1\ [mm]$, $R_y = \infty$ and $(m,n) = (1,1)(\overline{\omega}_L = \omega_L \mathrm{R}_x^2\sqrt{\frac{\rho}{E}}/h)$

	$\overline{\omega}_L$		$\frac{\omega_{NL}}{\omega_L}$	
V_{CNT}^*	Present	Ref. (Shen and Xiang 2014)	Present	Ref. (Shen and Xiang 2014)
		ΔT=300K		
0.12	18.3951	18.5407	1.5893	1.5934
0.17	23.0025	23.0831	1.5589	1.5620
0.28	26.4782	26.5256	1.6081	1.6441
		ΔT=400K		
0.12	15.0347	15.0663	1.8096	1.8109
0.17	18.7783	18.9391	1.7516	1.7584
0.28	21.5156	21.6385	1.8715	1.8736

stresses (including non-tensile stresses) change uniformly over the whole research region, in contrast to the findings of traditional finite element analysis, which clearly exhibit discontinuities. Neural network techniques are particularly well adapted to situations that need for high-order continuity of the displacement field (displacement derivative), for as in strain gradient elasticity theory. This is a related benefit. Using traditional finite element techniques may be challenging given the continuity requirement of C1. The inverse problem may also be handled by neural network systems since they can address both the forward and the inverse issues within the same framework. In the current study, the displacement field $\boldsymbol{u} = (u, \mathrm{v}, \mathrm{w})$ inside the analysis domain in the cylindrical coordinates $(x, y, z) \in V$ is solved using a fully connected neural network. A succession of completely linked layers make up the fully connected neural network, which links every neuron in one layer to every other neuron in the one below. The entirely connected architecture offers a wide range of applications since there are no special input assumptions. The deep neural network is shown in Fig. 3 operating as a

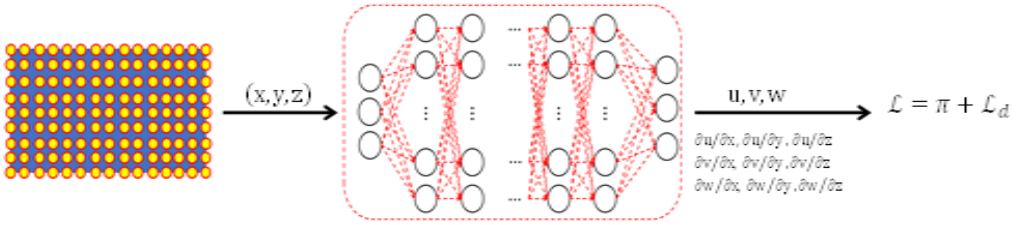

Fig. 1b A deep neural network acting as a surrogate mechanics model

substitute mechanical model. In this scenario, the deep neural network's inputs are the spatial coordinates (x, y, z), and its outputs are the displacements $\boldsymbol{u} = (u, \mathrm{v}, \mathrm{w})$. The neural network is supposed to have N-1 or (N) hidden layers. Mi neurons make up the i-th layer. The symbol $h_{j,i}^{out}$ denotes the output of the jth neuron in the ith layer as follows:

$$h_{j,i}^{out} = f\left(h_i^{in}\right), \quad with h_i^{in} = \sum_{m=1}^{M_{i-1}} w_{m,i} h_{m,i-1}^{out} + b_{j,i} \tag{42}$$

where $w_{m,i}$ stands for the weight and $b_{j,i}$ stands for the bias. The string $h_{m,i-1}^{out}$ out denotes the output of the $(i-1)$-th layer's mth neuron. f () is a representation of the nonlinear activation function. In both vector and matrix form, Eq. (22) may be written as follows:

$$\boldsymbol{h}_i = f(\boldsymbol{w}^{\mathrm{T}} \cdot \boldsymbol{h}_{i-1} + \boldsymbol{b}_i) \tag{43}$$

Finally, the neural network $(x, y, z) = NN(x, y, z)$ for solving the boundary value issue may be described as follows:

Input layer:

$$\boldsymbol{h}_0 = (x, y, z) \tag{44}$$

Hidden layer:

$$\mathbf{h}_i = f(\mathbf{w}^{\mathrm{T}} \cdot \mathbf{h}_{i-1} + \mathbf{b}_i), 1 \leqslant i \leqslant N-1 \tag{45}$$

Output layer

$$\mathbf{h}_N = \left(u_x, u_y\right) = \mathbf{w}^{\mathrm{T}} \cdot \mathbf{h}_{N-1} + \mathbf{b}_N \tag{46}$$

It's crucial to note that neural networks might theoretically approximate any function. The weight w^{T} and the ball bias are the parameters that are trained by minimizing the loss function, Eq. (46). To answer Eq. (46), a fully connected neural network is used in this study. The input and output layers, which are both 2×1 tensors, provide the spatial coordinates of the alignment points and the displacements that the DNN predicts. All layers make use of a sigmoid linear unit (SiLU) activation function, with the exception of the last layer, which is devoid of one. The partial derivatives of the displacements are computed using automated differentiation techniques, which are often utilized in physically influenced neural networks, with respect to their input coordinates. Using Monte Carlo integration, the overall energy loss for buildings with complicated shapes may be objectively assessed. A more accurate Gaussian quadrature method for the cylindrical structures expressly studied in this work will be presented in the following section. The DNN network is trained to minimize the loss function by integrating the total potential energy and displacement boundary contributions using an ADAM (adaptive momentum) optimizer and quasi-Newtonian (L) method. -BFG. The expected learning rate, unless otherwise specified, is 0.001. The neural network solution, or displacement field, ensures that the loss function satisfies the equilibrium criteria with the given boundary conditions while lowering the potential energy.

4.3 Parametric results

In this section, the influences of various parameters on the sensitivity of concrete structures' nonlinear frequency to GPLs reinforcement (SCS-GPLs) and sensitivity of concrete structures' nonlinear frequency to temperature (SCS-TEM). The SCS-GPLs and SCS-TEM can be formulated as follows:

$$\mathrm{SCS-GPLs} = \frac{f_{nl1} - f_{nl2}}{f_{nl1}}, \quad \mathrm{SCS-TEM} = \frac{f_{nl3} - f_{nl4}}{f_{nl3}} \tag{47}$$

In Eq. (47) f_{nl1}, f_{nl2} are the nonlinear frequencies with and without considering GPLs as the reinforcement, respectively. Also, f_{nl3}, f_{nl4} are the frequency in nonlinear form with and without considering temperature change, respectively. Also, in this section have $K_3 = 10^2\left(\frac{N}{m^5}\right)$, and $K_4 = 50\left(\frac{N}{m^7}\right)$. Also, in the work the boundary conditions of the structure are clamped in all edges. So, displacement fields are equal to zero in all edges.

4.3.1 Impacts of some parameters on the nonlinear to linear frequency of the current structure

The effects of the Winkler coefficient, temperature variations, and the weight percentage of GPLs on the nonlinear to linear frequency curves for different large deflection factors are shown in Fig. 2 in that order. Fig. 2-a shows the effects of three settings of the Winkler coefficient parameter on concrete panel nonlinear to linear frequency curves for various big deflection factors. As can be observed, a larger deflection factor enhances the structure's nonlinear to linear frequency curves. For the Winkler coefficient parameter, this problem is inverse. In a different universe, as the Winkler coefficient increases, the concrete structure's nonlinear frequency ratio declines. This indicates that this parameter has a higher effect on linear frequency than on nonlinear frequency. The findings of this Figure

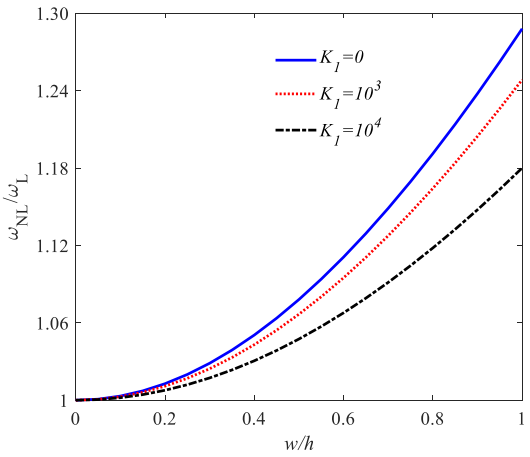

(a)

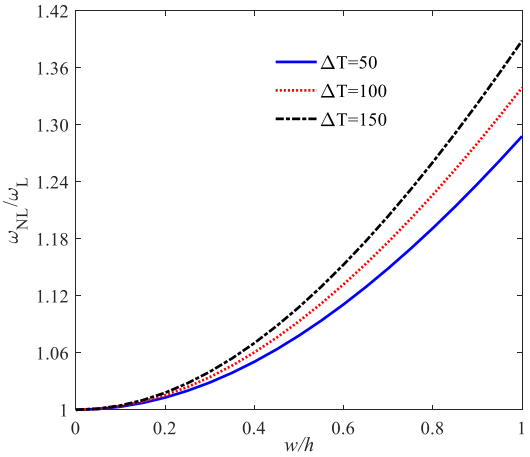

(b)

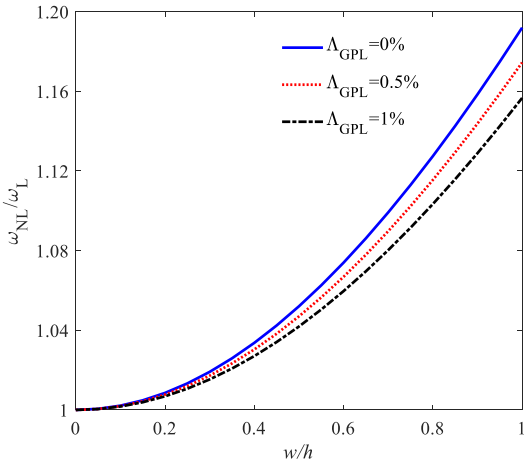

(c)

Fig. 2 The influences of GPLs' weight fraction, linear Winkler coefficient, and temperature change on the nonlinear to linear frequency of the current composite structure

unequivocally show that the nonlinear frequency ratio is more sensitive to a low value of significant deflection than a greater one. The impact of temperature variations and a dimensionless big deflection factor on the nonlinear to linear frequency curves of the structure in Fig. 2-b is the subject of the following discussion and analysis. It is

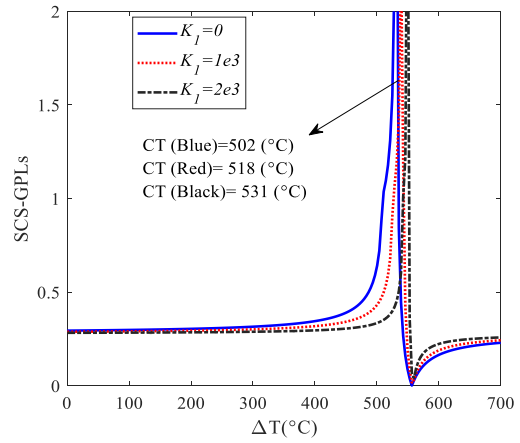

Fig. 3 The SCS-GPLs of the composite panel for different K_1, and ΔT

obvious that temperature variations have a greater impact on the linear frequency than the nonlinear one, comparable to Fig. 2-a. This indicates that the nonlinear frequency ratio increases with increasing temperature changes. The effect of the dimensionless huge deflection factor and the weight percentage of GPLs on the nonlinear to linear frequency curves of concrete structures is depicted in Fig. 2-c. This figure indicates that the nonlinear frequency change of the composite structure reduces as the weight percentage of GPLs increases. By contrasting the findings of the Figures, it can be said that the nonlinear frequency change lowers with an increase in the weight fraction of GPLs and the Winkler coefficient parameter, however, it rises with an increase in temperature changes.

4.3.2 Sensitivity of concrete structures to GPLs reinforcement

The influences of temperature change and linear Winkler coefficient on the SCS-GPLs are depicted in Fig. 3. As is observed, by increasing the temperature change, the SCS-GPLs increase. This increase continues till $502^{\circ}C$ for K_1=0. This value of temperature is called the critical temperature change of the structure. It means that after this value of temperature, the sensitivity of the system drops sharply. It should be mentioned that in the critical temperature of the structure, buckling occurs. It means that in this value of temperature change, buckling occurs. As is presented, by increasing the linear Winkler coefficient the sensitivity of the concrete structure to the nanocomposites decreases. This decrease is obviously seen especially in the temperature near the thermal buckling load. It is clearly observed that after the thermal buckling load, the structure sharply decreases till the thermal post-buckling load. It should be noted that the thermal post-buckling load is not dependent on the linear Winkler coefficient. The reason for this issue is that the linear Winkler coefficient did not appear in the nonlinear frequency of the system. It should be noted that the thermal buckling for K_1 = 0, 10^3, and 2×10^3 are $502^{\circ}C$, $518^{\circ}C$ and $531^{\circ}C$, respectively. Finally, it is worth mentioning that all designers for modeling the concrete structure reinforced by GPLs should pay special attention to the lower values of temperature especially those lower than $500^{\circ}C$.

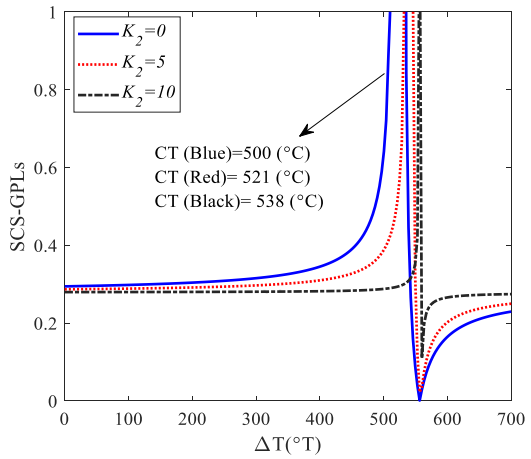

Fig. 4 The SCS-GPLs of the composite panel for different K_2, and ΔT

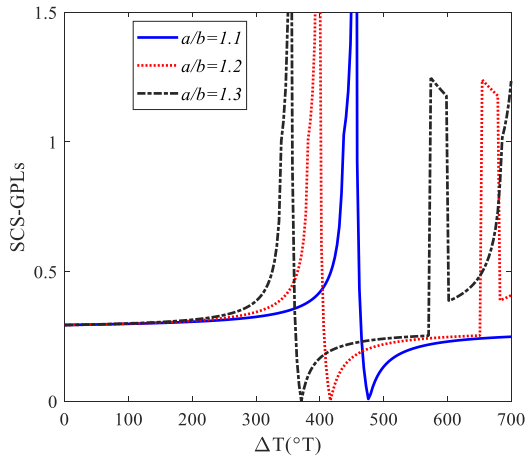

Fig. 5 The variation of SCS-GPLs for different *a/b*, and ΔT

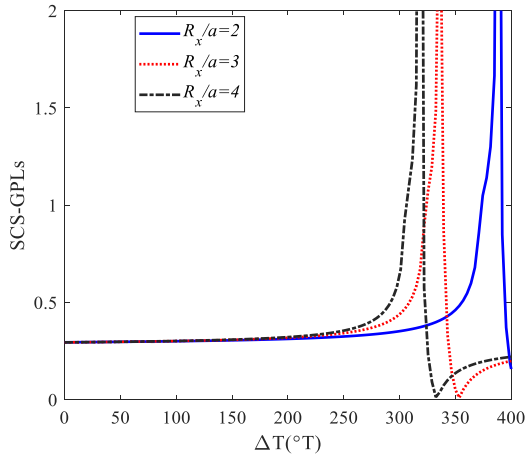

Fig. 6 The variation of SCS-GPLs for different R_x/a, and ΔT

Fig. 4 shows the effects of temperature variation and the Pasternak coefficient on the SCS-GPLs. As can be seen, the SCS-GPLs rise as the temperature change increases. For K_2=0, the rise lasts until 500° C. This temperature is referred to as the structure's critical temperature change. This indicates that the system's sensitivity reduces significantly below this temperature. It should be noted that buckling happens when the structure reaches its critical temperature. This indicates that buckling happens at this level of temperature fluctuation. As shown, the susceptibility of the concrete structure to the nanocomposites reduces as the Pasternak coefficient rises. This drop in temperature is particularly noticeable when it is close to the thermal buckling load. It is evident that the structure rapidly declines until thermal post-buckling stress follows thermal buckling force. It should be noted that the Pasternak coefficient has no influence on the thermal post-buckling load. This problem results from the absence of the Pasternak coefficient in the system's nonlinear frequency. It should be noticed that K_2=0, 5, and 10 have thermal buckling at 500° C, 521° C, and 538° C, respectively.

The influences of *a/b*, and temperature change on the SCS-GPLs can be seen in Figure 5. Generally, when a structure encounters a sharp increase or decrease in the frequency due to increasing temperature change, buckling occurs. So, in this capture, as is observed, by increasing the temperature, the sensitivity of the current concrete structure to the GPLs increases. After this increase, we see a sharp decrease in the SCS-GPL in the structure due to increasing the temperature change. In this temperature buckling happens. In other work, by increasing the *a/b* parameter, the thermal buckling decreases. After thermal buckling, the structure encounters instability in response and the designers should pay special attention to the stable area.

Fig. 6 illustrates the effects of temperature variation and R_x/a on the SCS-GPLs. Buckling often happens when a structure has a sudden rise or fall in frequency owing to an increase in temperature change. As a result, it can be seen in this picture that as the temperature rises, the present concrete structure becomes more sensitive to GPLs. As the temperature changes further after this, we see a dramatic drop in the SCS-GPL in the structure. Buckling occurs in this temperature range. In other research, the thermal buckling is reduced by raising the R_x/a value. The structure experiences instability as a result of thermal buckling, thus the designers must pay close attention to the stable region.

4.3.3 Sensitivity of concrete structures to temperature (SCS-TEM)

The influence of length-to-width ratio (*a/b*), and GPL weight fraction on the sensitivity of the structure on the temperature has been presented in Fig. 7. As is observed, in $\Delta T = 150°$ C, by increasing the length-to-width ratio, the sensitivity of the structure to the temperature increases especially in the lower values of *a/b* (less than 6). As an amazing result, in the higher values of *a/b*, the sensitivity of the structure to temperature becomes constant. It means that the structure in the higher values of *a/b* (higher than 6) is not sensitive to the temperature ($\Delta T = 150°$ C). An amazing result can be seen in Fig. (6. b). In the higher temperature than Fig. (7. a), the sensitivity of the structure to the temperature changes. It means that in $\Delta T = 155°$ C, by increasing the *a/b* parameter, the SCS-TEM increases sharply, but in a specific *a/b*, a sharp decrease can be seen in the system. It means that the system encounters

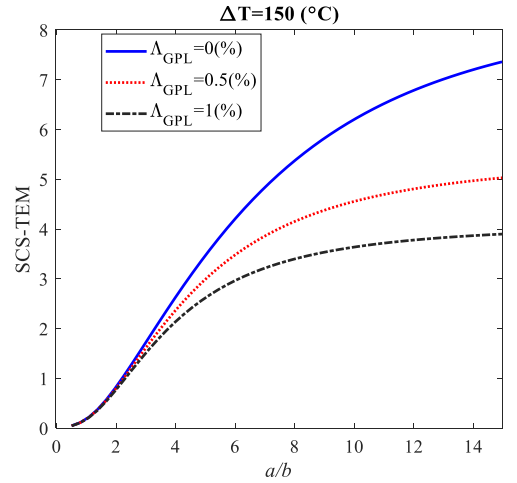

(a)

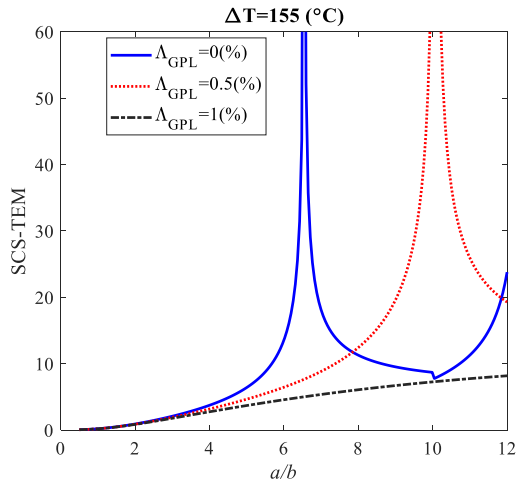

(b)

Fig. 7 The variation of SCS-TEM for different GPLs' weight fraction, a/b and ΔT

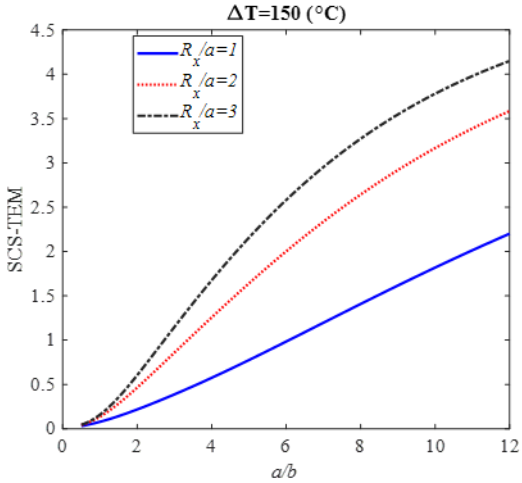

(a)

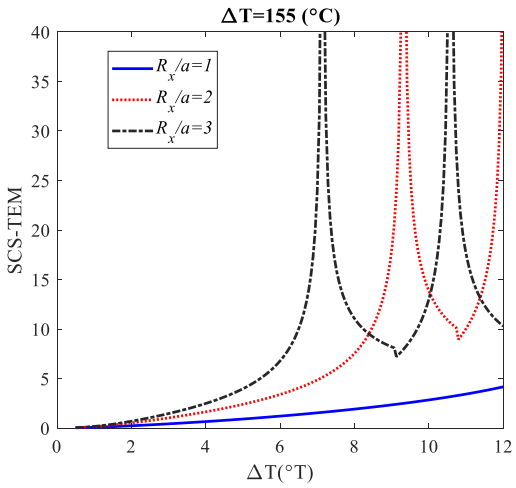

(b)

Fig. 8 The variation of SCS-TEM for different R_x/a, a/b, and ΔT

instability in response to the higher values of a/b. Also, by increasing the GPLs' weight fraction, the sensitivity of the structure to the temperature decreases especially in the higher values of a/b parameter. All designers in the higher values of ΔT should pay special attention to the value of a/b parameter.

In Fig. 8, the effect of the length-to-width ratio (a/b) and the R_x/a on the structure's susceptibility to temperature is shown. As can be seen, at ΔT=150° C, as the length-to-width ratio grows, so does the structure's sensitivity to temperature, especially for lower values of a/b (less than 6). Amazingly, the sensitivity of the structure to temperature becomes constant at the higher levels of a/b. It implies that the structure at higher a/b ratios (greater than 6) is not temperature-sensitive (ΔT=150° C). Figure (8. B) shows an incredible outcome. The susceptibility of the structure to temperature changes increases at higher temperatures than in Fig. 8.a. Increasing the a/b parameter causes the SCS-TEM to drastically grow at ΔT=155° C, however at a certain a/b, the system may be shown to dramatically decline. This indicates that the system experiences instability as a result of greater values of a/b. Additionally, by increasing the R_x/a, the structure becomes less sensitive to temperature, especially at higher values of the R_x/a parameter.

Fig. 9 shows the effects of a/b, R_y/b, and ΔT on the sensitivity of the existing concrete structure. SCS-TEM increases with increasing a/b in the lower values of a/b and with rising a/b in ΔT equal to 100° C. This increment turns into a constant number for a/b greater than 6. It indicates that the system is less susceptible to temperature at higher a/b values by increasing the length-to-width ratio. The existing concrete system's temperature sensitivity is dependent on the a/b parameter when the Ry/b is increased. It indicates that the system's sensitivity to temperature rises with increasing R_y/b at ΔT = 100° C and smaller values of a/b (less than 3.9). As the trend toward increasing a/b levels turns reversed. As is observed in Fig. (9. b), by increasing the ΔT to 150° C, we cannot increase the a/b parameter. It means that for obtaining the stable response, the value of a/b parameter should be less than 4 for R_y/b equal to 1.

To understand the impacts of K_1, and a/b parameters on the SCS-TEM, Fig. 10 has appeared. According to this image, in the lower values of a/b, K_1 parameter does not

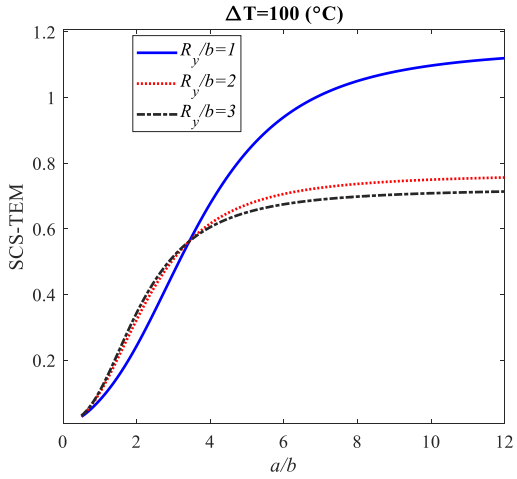

(a)

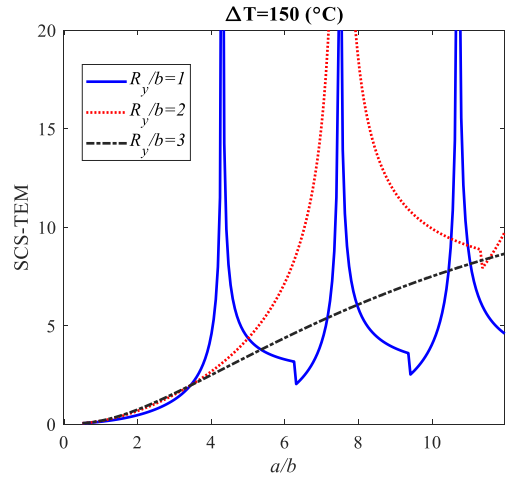

(b)

Fig. 9 The variation of SCS-TEM for different R_y/a, a/b, and ΔT

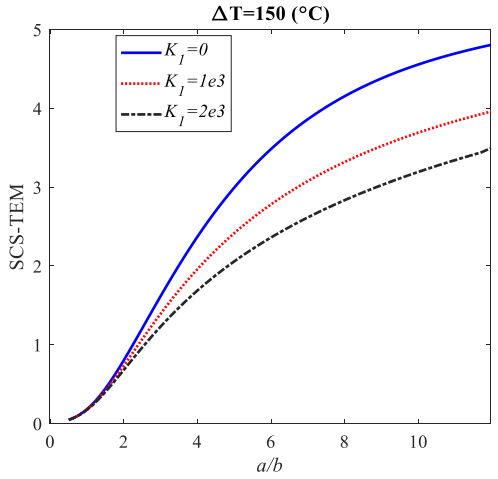

(a)

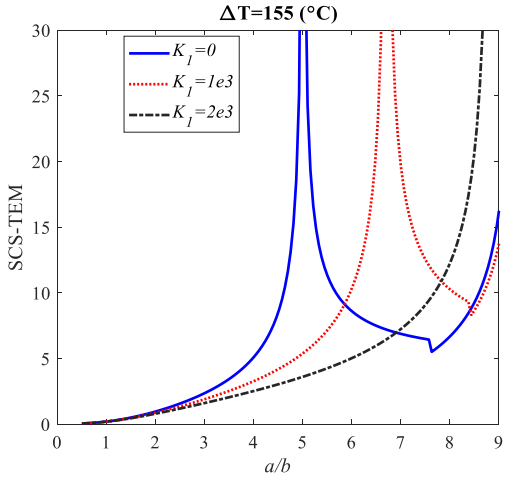

(b)

Fig. 10 The variation of SCS-TEM for different K_1, a/b, and ΔT

have any influence on the SCS-TEM. But, in the higher values of a/b, by increasing the K_1 parameter, the sensitivity of the nonlinear frequency to the temperature decreases. In the lower values of K_1 parameter, for modeling a structure should pay special attention to the value of a/b. Also, in ΔT equal to 155° C, by increasing the K_1 parameter, designers can select higher values of a/b in comparison with lower values of K_1 parameter. Also, by increasing the ΔT, the intensity of the sensitivity of the current composite structure to the a/b increases.

Fig. 11 has been published in order to better understand the effects of K_2, and the a/b parameters on the SCS-TEM. This figure shows that the K_1 parameter has little effect on the SCS-TEM at the lower levels of a/b. However, if the K_2 parameter is increased, the sensitivity of the nonlinear frequency to temperature diminishes for larger values of a/b. The value of a/b should get particular consideration when modeling a structure at lower K_2 parameter levels. Additionally, designers may choose greater values of a/b in ΔT equal to 155 by raising the K_2 parameter as opposed to smaller values of K_2. Additionally, when ΔT is raised, the existing composite structure's sensitivity to a/b becomes more intense.

4.4 The results of the mentioned data-driven solution

The aforementioned DNN has 6, 8, 5, 7, 5, 3, 5, 6, 7 neurons, with 9 neurons in the input layer and 1 neuron in the output layer. The number of neurons in each hidden layer is represented by other numbers. A back-propagation optimization forward network makes up the proposed artificial neural network (ANN). The optimum loss function for this regression issue is a mean square error (MSE), which is defined as follows:

$$MSE_j = \frac{1}{n}\sum_{i=1}^{n}\left(Y_{ji} - \widehat{Y_{ji}}\right)^2 \tag{48}$$

ANN is used to compare all expected outcomes to actual occurrences, allowing predictions to be formed for all outcomes. Also interesting is the conversion of dynamic response to a real value depending on their stiffness. According to section 5.2, known output and input parameters are utilized to extract a set of 189 data using the numerical results. While this data includes both left and right boundary conditions, for the sake of our problem, only two BCs—strict -strict and basic BC supported—are taken into account. Based on the numerical outcomes, other substrate

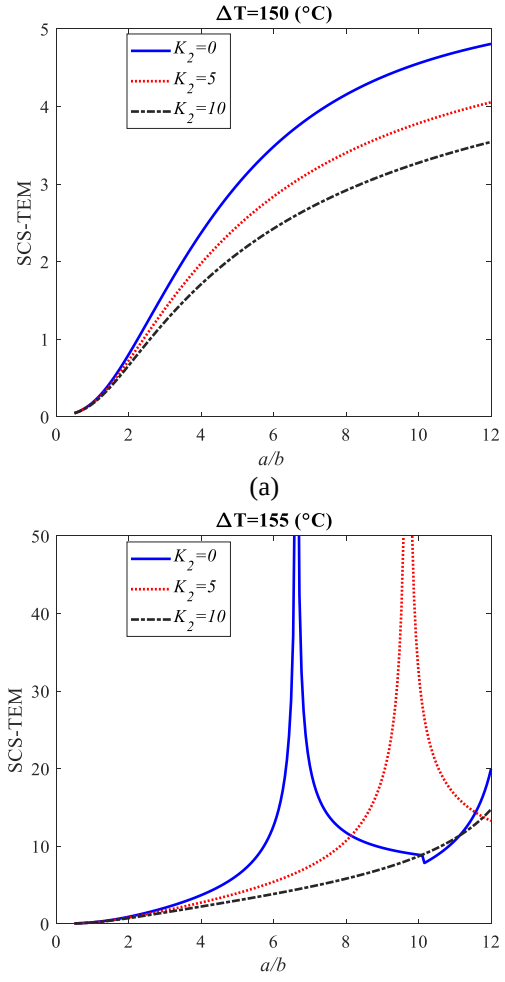

Fig. 11 The variation of SCS-TEM for different K_2, a/b, and ΔT

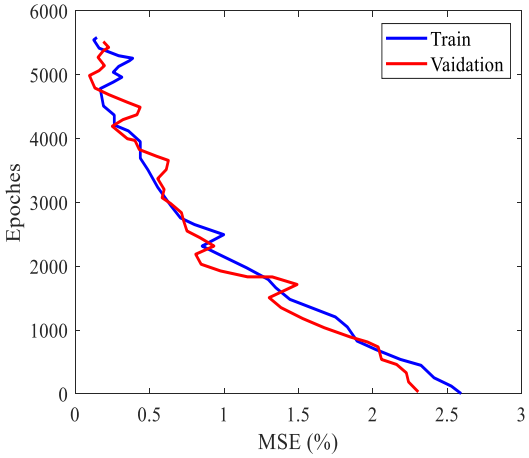

Fig. 12 The determined MSE value by counting the number of epochs for each output from the validation and train sets of data

data quantities, external voltage, etc. are determined. However, the numerical data in Figs. 2-11 is used to determine the output values for amplitude and bending information. The PyTorch IANN training method is rather

Table 3 The prediction of the DNN model's performance in relation to test data for different MSN parameters and dynamical load to determine the nonlinear frequency (GHz) of the present structure

		Predicted		
	Fit	$MSE_{Train} = 2.13 \times 10^{-4}$	$MSE_{Train} = 3.1 \times 10^{-4}$	$MSE_{Train} = 3.4 \times 10^{-4}$
		K2=0.100		
K1=0	0.0569	0.035821	0.056528	0.056895
K1=10^2	0.07152	0.051258	0.069196	0.071499
K1=10^3	0.09125	0.081258	0.085698	0.091118
		K2=200		
K1=0	0.08158	0.068512	0.079528	0.081499
K1=10^2	0.09859	0.074589	0.095258	0.098412
K1=10^3	0.11258	0.087458	0.099369	0.111590

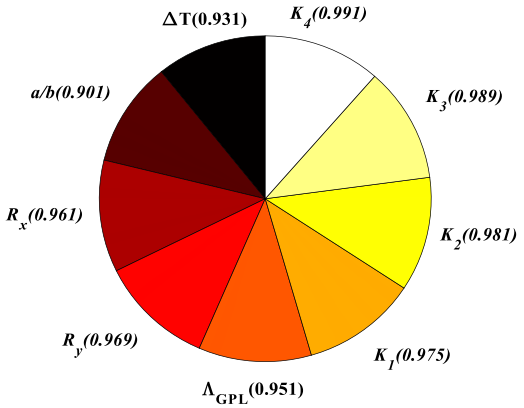

Fig. 13 The input variables' sensitivity analysis

simple. The gathered data is randomly divided into three halves for the network's training, validation, and testing stages. The number of network epochs (or iterations) to utilize is determined by the value of the loss function. The training data make up 80% of the dataset, while the validation and testing data make up the remaining 40% equally. The quantity of epochs needed for training and validation data is shown in Fig. 12. Typically, the network may be regarded as trained if the difference in the number of pre-start epochs in the loss-error curve between training and validation is detected. Even if the training error goes down after this number of epochs, the network is overfitted and only works well with the training data set. The IANN will provide inflated and false findings for the validation data set and all subsequent input data. As we have shown, 3800 epochs are necessary in order to have confidence in the outcome. This amount of epoch size will prevent the amplitude from being overfitted.

Table 3 indicates that we should take into account $MSE_{Train} = 3.4 \times 10^{-4}$, in order to verify the outcomes of the present work with the outputs of DNN. The findings are confirmed, as can be observed by choosing this number for DNN. Other evidence in Table 3 demonstrates that the nonlinear frequency of the current system rises with increasing Winkler and Pasternak coefficients.

The aforementioned algorithm's sensitivity results were assessed, and Yang *et al.*'s approach (Yang and Zhang 1997) was used to determine how input variables influenced the output data. The Eq. below is used in this tactic:

$$\exists_{ij}=\frac{\sum_{k=1}^{n}(\cap_i\times\ni_j)}{\sqrt{\sum_{k=1}^{n}\cap_i{}^2\sum_{k=1}^{n}\ni_j{}^2}} \quad (49)$$

Each of the input and output variables, $\cap$ and $\ni$, has 380 possible values. Each input parameter has a value between 0 and 1, with the greatest value corresponding to the most effective output $\exists$ variable. Fig. 13 displays the $\exists$ ratings for each input variable. The K_4 ($\exists$ = 0.991) has the greatest impact on the outcomes of the aforementioned operation, as seen in Fig. 13.

5. Conclusions

When the amplitude of the vibrations is similar to that of the clearance, the vibrations for small amplitudes were really substantially nonlinear. The consequences of the von Kármán strain-displacement kinematic nonlinearity on the constitutive laws of the shell were given in the current study using 3D modeling of the shell theory. The nonlinear governing equations. for various nonlinear boundary edges were solved by discretizing equations on the space domain, constructing equations of the Duffing type, and using Kronecker and Hadamard products. Thermo-elasticity equations were used to simulate the system's temperature. The harmonic solution technique for the displacement domain and the multiple-scale approach for the time domain were provided in the section on solution procedures for solving nonlinear Equations. It was often utilized to predict how diverse systems would behave using the effective data-driven approach. The network's hyperparameters, such as the number of hidden layers and learning rate, were often chosen manually as required. Additionally, a data-driven solution to the nonlinear vibration issue was proposed in order to reduce the computational cost of the current study. The findings might be confirmed by comparing the outcomes of the present effort with those of data-driven solutions and another research that was published. For building construction industries, several useful recommendations for improving the thermo-mechanics' behavior of structural concrete panels were presented. The results section presented the following information:

• the nonlinear frequency change lowers with an increase in the weight fraction of GPLs and the Winkler coefficient parameter, however, it rises with an increase in temperature changes.

• all designers for modeling the concrete structure reinforced by GPLs should pay special attention to the lower values of temperature especially those lower than $500^{\circ}C$.

• by increasing the temperature, the sensitivity of the current concrete structure to the GPLs increases.

• According to the results of sensitivity analysis, the thermal buckling is reduced by raising the R_x/a value.

• All designers in the higher values of ΔT should pay special attention to the value of a/b parameter.

• by increasing the R_x/a, the structure becomes less sensitive to temperature, especially at higher values of the R_x/a parameter.

• By increasing the R_y/b, the sensitivity of the current concrete system to the temperature depends on the a/b parameter.

The analysis of current work in the aerodynamics situation, under low-velocity impact loading, under wind excitation, and under thermal shock can be presented in the future scope of the study.

Acknowledgment

The authors extend their appreciation to King Saud University for funding this work through Researchers Supporting Project number (RSPD2024R711), King Saud University, Riyadh, Saudi Arabia.

References

Alazwari, M.A., Daikh, A.A. and Eltaher, M.A. (2022a), "Novel quasi 3D theory for mechanical responses of FG-CNTs reinforced composite nanoplates", *Adv. Nano Res.*, **12**(2), 117. https://doi.org/10.12989/anr.2022.12.2.117.

Alazwari, M.A., Esen, I., Abdelrahman, A.A., Abdraboh, A.M. and Eltaher, M.A. (2022b), "Dynamic analysis of functionally graded (FG) nonlocal strain gradient nanobeams under thermo-magnetic fields and moving load", *Adv. Nano Res.*, **12**(3), 231-251. https://doi.org/10.12989/anr.2022.12.3.231.

Amelirad, O. and Assempour, A. (2019), "Experimental and crystal plasticity evaluation of grain size effect on formability of austenitic stainless steel sheets", *J. Manuf. Proc.*, **47**, 310-323. https://doi.org/10.1016/j.jmapro.2019.09.035

Babaei, M., Atasoy, A., Hajirasouliha, I., Mollaei, S. and Jalilkhani, M. (2022), "Numerical solution of beam Eq. using neural networks and evolutionary optimization tools", *Adv. Comput. Des.*, **7**(1), 1-17. https://doi.org/10.12989/acd.2022.7.1.001

Bidzard, A., Malekzadeh, P. and Mohebpour, S.R. (2022), "A size-dependent nonlinear finite element free vibration analysis of multilayer FG-GPLRC toroidal micropanels in thermal environment", *Compos. Struct.*, **279**, 114783. https://doi.org/10.1016/j.compstruct.2021.114783

Chen, L., Chen, Z., Xie, Z., Wei, L., Hua, J., Huang, L. and Yap, P.S. (2023), "Recent developments on natural fiber concrete: A review of properties, sustainability, applications, barriers, and opportunities", *Develop. Built Environ.*, **16**, 100255. https://doi.org/10.1016/j.dibe.2023.100255

Chen, L., Yang, H., Song, K., Huang, W., Ren, X. and Xu, H. (2021), "Failure mechanisms and characteristics of the Zhongbao landslide at Liujing Village, Wulong, China", *Landslides*, **18**(4), 1445-1457. https://doi.org/10.1007/s10346-020-01594-1

Cui, C., Nie, T., Zhou, B., Cai, Y., Wang, G., Bai, J., Wang, H. and Ma, S. (2021), "Preparation and investigation of graphene-coated lead-free glass frit based on amino dispersant for improved adhesion and lower temperature point", *Diamond Relat. Mater.*, **11**, 108213, https://doi.org/10.1016/j.diamond.2020.108213.

Dai, Z., Xie, J. and Jiang, M. (2023), "A coupled peridynamics–smoothed particle hydrodynamics model for fracture analysis of fluid–structure interactions", *Ocean Eng.*, **279**, 114582. https://doi.org/10.1016/j.oceaneng.2023.114582

Fan, L., Sahmani, S. and Safaei, B. (2021), "Couple stress-based dynamic stability analysis of functionally graded composite truncated conical microshells with magnetostrictive facesheets embedded within nonlinear viscoelastic foundations", *Eng. Comput.*, **37**, 1635-1655. https://doi.org/10.1007/s00366-020-01182-w

Fazzolari, F.A. and Carrera, E. (2013), "Free vibration analysis of sandwich plates with anisotropic face sheets in thermal environment by using the hierarchical trigonometric Ritz formulation", *Compos. Part B Eng.*, **50**, 67-81. https://doi.org/10.1016/j.compositesb.2013.01.020

Fei, Y., Fang, S. and Hu, Y.H. (2020), "Synthesis, properties and potential applications of hydrogenated graphene", *Chem. Eng. J.*, **397**, 125408, https://doi.org/10.1016/j.cej.2020.125408.

Feng, J., Safaei, B., Qin, Z. and Chu, F. (2023), "Nature-inspired energy dissipation sandwich composites reinforced with high-friction graphene", *Compos. Sci. Technol.*, **233**, 109925. https://doi.org/10.1016/j.compscitech.2023.109925

Feng, Y., Mohammadi, M., Wang, L., Rashidi, M. and Mehrabi, P. (2021), "Application of artificial intelligence to evaluate the fresh properties of self-consolidating concrete", *Materials*, **14**(17), 4885. https://doi.org/10.3390/ma14174885

Firouzianhaji, A., Usefi, N., Samali, B. and Mehrabi, P. (2021), "Shake table testing of standard cold-formed steel storage rack", *Appl. Sci.*, **11**(4), 1821. https://doi.org/10.3390/app11041821

Frostig, Y. and Thomsen, O.T. (2009), "On the free vibration of sandwich panels with a transversely flexible and temperature-dependent core material–Part I: Mathematical formulation", *Compos. Sci. Technol.*, **69**(6), 856-862. https://doi.org/10.1016/j.compscitech.2008.03.003.

Gaj, J., Clapa, M., Nowak, D., Juszczak, J., Galazka, M., Pelka, M. and Niedzielski, P. (2020), "Metallurgical graphene under different gas atmospheres and UV radiation for gas-sensing applications", *Sensors Actuat. A Phys.*, **312**, 112152. https://doi.org/10.1016/j.sna.2020.112152.

Guo, J., Baharvand, A., Tazeddinova, D., Habibi, M., Safarpour, H., Roco-Videla, A. and Selmi, A. (2022), "An intelligent computer method for vibration responses of the spinning multi-layer symmetric nanosystem using multi-physics modeling", *Eng. Comput.*, **38**(Suppl5), 4217-4238. https://doi.org/10.1007/s00366-021-01433-4

Guo, X., Liu, Y. and Wang, G. (2021), "Computer modeling for frequency performance of viscoelastic magneto-electro-elastic annular micro/nanosystem via adaptive tuned deep learning neural network optimization", *Advances in nano research*. **11**(2), 203, https://doi.org/10.12989/anr.2021.11.2.203

Han, S., Zheng, D., Mehdizadeh, B., Nasr, E.A., Khandaker, M.U., Salman, M. and Mehrabi, P. (2023a), "Sustainable design of self-consolidating green concrete with partial replacements for cement through neural-network and fuzzy technique", *Sustainability*, **15**(6), 4752. https://doi.org/10.3390/su15064752

Han, S., Zhu, Z., Mortazavi, M., El-Sherbeeny, A.M. and Mehrabi, P. (2023b), "Analytical assessment of the structural behavior of a specific composite floor system at elevated temperatures using a newly developed hybrid intelligence method", *Buildings*, **13**(3), 799. https://doi.org/10.3390/buildings13030799

Han, Y., Shao, S., Fang, B., Shi, T., Zhang, B., Wang, X. and Zhao, X. (2023c), "Chloride ion penetration resistance of matrix and interfacial transition zone of multi-walled carbon nanotube-reinforced concrete", *J. Build. Eng.*, **72**, 106587. https://doi.org/10.1016/j.jobe.2023.106587

Hao, R.B., Lu, Z.Q., Ding, H. and Chen, L.Q. (2022), "A nonlinear vibration isolator supported on a flexible plate: analysis and experiment", *Nonlinear Dyn.*, **108**(2), 941-958. https://doi.org/10.1007/s11071-022-07243-7.

HB, K. (1977), "Numerical Solution of Bifurcation and Nonlinear Eigenvalue Problem", *Appl. Bifurcat. Theor.*

He, H., Wang, S., Shen, W. and Zhang, W. (2023), "The influence of pipe-jacking tunneling on deformation of existing tunnels in soft soils and the effectiveness of protection measures", *Transport. Geotech.*, **42** 101061. https://doi.org/10.1016/j.trgeo.2023.101061.

Houari, M.S.A., Tounsi, A. and Bég, O.A. (2013), "Thermoelastic bending analysis of functionally graded sandwich plates using a new higher order shear and normal deformation theory", *Int. J. Mech. Sci.*, **76**, 102-111. https://doi.org/10.1016/j.ijmecsci.2013.09.004

Hu, D., Sun, H., Mehrabi, P., Ali, Y.A. and Al-Razgan, M. (2023), "Application of artificial intelligence technique in optimization and prediction of the stability of the walls against wind loads in building design", *Mech. Adv. Mater. Struct.*, 1-18. https://doi.org/10.1080/15376494.2023.2206208

Huang, H., Yuan, Y., Zhang, W. and Zhu, L. (2021), "Property assessment of high-performance concrete containing three types of fibers", *Int. J. Concr. Struct. Mater.*, **15**(1), 1-17. https://doi.org/10.1186/s40069-021-00476-7

İnada, A.A., Arman, S. and Safaei, B. (2022), "A novel review on the efficiency of nanomaterials for solar energy storage systems", *J. Energy Storage*, **55**, 105661. https://doi.org/10.1016/j.est.2022.105661

Khalili, S.M.R. and Mohammadi, Y. (2012), "Free vibration analysis of sandwich plates with functionally graded face sheets and temperature-dependent material properties: A new approach", *Eur. J. Mech. A Solids*, **35**, 61-74. https://doi.org/10.1016/j.euromechsol.2012.01.003.

Kuang, W., Wang, H., Li, X., Zhang, J., Zhou, Q. and Zhao, Y. (2018), "Application of the thermodynamic extremal principle to diffusion-controlled phase transformations in Fe-CX alloys: Modeling and applications", *Acta Materialia*. **159** 16-30. https://doi.org/10.1016/j.actamat.2018.08.008

Kulikov, G.M. and Plotnikova, S.V. (2015), "Three-dimensional thermal stress analysis of laminated composite plates with general layups by a sampling surfaces method", *Eur. J. Mech. A Solids*, **49**, 214-226. https://doi.org/10.1016/j.euromechsol.2014.07.011

Li, X., Zhu, H. and Yuan, Q. (2023), "Dilatancy Eq. based on the property-dependent plastic potential theory for geomaterials", *Fractal Fraction.*, **7**(11), 824. https://doi.org/10.3390/fractalfract7110824

Li, Z.M., Liu, T. and Qiao, P. (2021), "Nonlinear vibration and dynamic instability analyses of laminated doubly curved panels in thermal environments", *Compos. Struct.*, **267**, 113434. https://doi.org/10.1016/j.compstruct.2020.113434

Lin, J.X., Chen, G., Pan, H.S., Wang, Y.C., Guo, Y.C. and Jiang, Z.X. (2023), "Analysis of stress-strain behavior in engineered geopolymer composites reinforced with hybrid PE-PP fibers: A focus on cracking characteristics", *Compos. Struct.*, **323**, 117437. https://doi.org/10.1016/j.compstruct.2023.117437

Liu, B., Yang, H. and Karekal, S. (2020), "Effect of water content on argillization of mudstone during the tunnelling process", *Rock Mech. Rock Eng.*, **53**, 799-813. https://doi.org/10.1007/s00603-019-01947-w

Liu, C., Cui, J., Zhang, Z., Liu, H., Huang, X. and Zhang, C. (2021), "The role of TBM asymmetric tail-grouting on surface settlement in coarse-grained soils of urban area: Field tests and FEA modelling", *Tunnell. Undergr. Space Technol.*, **111**, 103857. https://doi.org/10.1016/j.tust.2021.103857

Liu, J., Mohammadi, M., Zhan, Y., Zheng, P., Rashidi, M. and Mehrabi, P. (2021), "Utilizing artificial intelligence to predict the superplasticizer demand of self-consolidating concrete incorporating pumice, slag, and fly ash powders", *Materials*, **14**(22), 6792. https://doi.org/10.3390/ma14226792

Liu, L., Lv, B. and He, T. (2015), "The stochastic dynamic snap-through response of thermally buckled composite panels",

Compos. Struct., **131**, 344-355. https://doi.org/10.1016/j.compstruct.2015.05.032

Lu, Z.Q., Gu, D.H., Ding, H., Lacarbonara, W. and Chen, L.Q. (2020), "Nonlinear vibration isolation via a circular ring", *Mech. Syst. Signal Pr.*, **136**, 106490. https://doi.org/10.1016/j.ymssp.2019.106490

Lu, Z., Yang, T., Brennan, M.J., Liu, Z. and Chen, L.-Q. (2017), "Experimental investigation of a two-stage nonlinear vibration isolation system with high-static-low-dynamic stiffness", *J. Appl. Mech.*, **84**(2), 021001. https://doi.org/10.1115/1.4034989

Ma, L.S. and Lee, D.W. (2012), "Exact solutions for nonlinear static responses of a shear deformable FGM beam under an in-plane thermal loading", *Eur. J. Mech. A Solids*, **31**(1), 13-20. https://doi.org/10.1016/j.euromechsol.2011.06.016

Matsunaga, H. (2007), "Free vibration and stability of angle-ply laminated composite and sandwich plates under thermal loading", *Compos. Struct.*, **77**(2), 249-262. https://doi.org/10.1016/j.compstruct.2005.07.002

Mehrabi, P., Honarbari, S., Rafiei, S., Jahandari, S. and Alizadeh Bidgoli, M. (2021), "Seismic response prediction of FRC rectangular columns using intelligent fuzzy-based hybrid metaheuristic techniques", *J. Ambient Intell. Human. Comput.*, **12**, 10105-10123. https://doi.org/10.1007/s12652-020-02776-4

Mehrabi, P., Shariati, M., Kabirifar, K., Jarrah, M., Rasekh, H., Trung, N.T., Shariati, A. and Jahandari, S. (2021), "Effect of pumice powder and nano-clay on the strength and permeability of fiber-reinforced pervious concrete incorporating recycled concrete aggregate", *Constr. Build. Mater.*, **287**, 122652. https://doi.org/10.1016/j.conbuildmat.2021.122652

Ming, Y., Zandi, Y., Gholizadeh, M., Oslub, K., Khadimallah, M.A. and Issakhov, A. (2021), "Computer simulation for stability performance of sandwich annular system via adaptive tuned deep learning neural network optimization", *Adv. Nano Res.*, **11**(1), 083, https://doi.org/10.12989/anr.2021.11.1.083

Moradi, H., Atashi, P., Amelirad, O., Yang, J.-K., Chang, Y.-Y. and Kamranifard, T. (2022), "Machine learning modeling and DOE-assisted optimization in synthesis of nanosilica particles via Stöber method", *Adv. Nano Res.*, **12**(4), 387. https://doi.org/10.12989/anr.2022.12.4.387

Pandey, S. and Pradyumna, S. (2015), "Free vibration of functionally graded sandwich plates in thermal environment using a layerwise theory", *Eur. J. Mech. A Solids*, **51**, 55-66. https://doi.org/10.1016/j.euromechsol.2014.12.001

Rafiee, M.A., Rafiee, J., Wang, Z., Song, H., Yu, Z.Z. and Koratkar, N. (2009), "Enhanced mechanical properties of nanocomposites at low graphene content", *ACS Nano*, **3**(12), 3884-3890, https://doi.org/10.1021/nn9010472.

Rao, R., Sahmani, S. and Safaei, B. (2021), "Isogeometric nonlinear bending analysis of porous FG composite microplates with a central cutout modeled by the couple stress continuum quasi-3D plate theory", *Arch. Civil Mech. Eng.*, **21**(3), 98. https://doi.org/10.1007/s43452-021-00250-2

Ren, C., Yu, J., Zhang, C., Liu, X., Zhu, Y. and Yao, W. (2023a), "Micro–macro approach of anisotropic damage: a semi-analytical constitutive model of porous cracked rock", *Eng. Fract. Mech.*, **290**, 109483. https://doi.org/10.1016/j.engfracmech.2023.109483

Ren, Z., Zeng, H., Zeng, X., Chen, X. and Wang, X. (2023b), "Effect of nanographite conductive concrete mixed with magnetite sand excited by different alkali activators and their combinations on the properties of conductive concrete", *Buildings*, **13**(7), 1630. https://doi.org/10.3390/buildings13071630

Safaei, B. (2021), "Frequency-dependent damped vibrations of multifunctional foam plates sandwiched and integrated by composite faces", *Eur. Phys. J. Plus*, **136**(6), 1-16. https://doi.org/10.1140/epjp/s13360-021-01632-4

Safaei, B., Onyibo, E.C., Goren, M., Kotrasova, K., Yang, Z., Arman, S. and Asmael, M. (2023), "Free vibration investigation on RVE of proposed honeycomb sandwich beam and material selection optimization", *Facta Univ. Series Mech. Eng.*, **21**(1), 031-050. https://doi.org/10.22190/FUME220806042S

Sahmani, S. and Safaei, B. (2021), "Microstructural-dependent nonlinear stability analysis of random checkerboard reinforced composite micropanels via moving Kriging meshfree approach", *Eur. Phys. J. Plus*, **136**, 1-31. https://doi.org/10.1140/epjp/s13360-021-01706-3

Sarkon, G.K., Safaei, B., Kenevisi, M.S., Arman, S. and Zeeshan, Q. (2022), "State-of-the-art review of machine learning applications in additive manufacturing, from design to manufacturing and property control", *Arch. Comput. Meth. Eng.*, **29**(7), 5663-5721. https://doi.org/10.1007/s11831-022-09786-9

Shen, H.S. and Xiang, Y. (2014), "Nonlinear vibration of nanotube-reinforced composite cylindrical panels resting on elastic foundations in thermal environments", *Compos. Struct.*, **111**, 291-300. https://doi.org/10.1016/j.compstruct.2014.01.010

Shi, M.L., Lv, L. and Xu, L. (2023), "A multi-fidelity surrogate model based on extreme support vector regression: Fusing different fidelity data for engineering design", *Eng. Comput.*, **40**(2), 473-493. https://doi.org/10.1108/EC-10-2021-0583

Shu, Z., Ning, B., Chen, J., Li, Z., He, M., Luo, J. and Dong, H. (2023), "Reinforced moment-resisting glulam bolted connection with coupled long steel rod with screwheads for modern timber frame structures", *Earthq. Eng. Struct. Dyn.*, **52**(4), 845-864. https://doi.org/10.1002/eqe.3789

Sobhani, E. (2023a), "Improvement of vibrational characteristics of multipurpose structures (plate and shells) used in aerospace components by deploying Graphene Oxide Powders (GOPs) in a matrix as a nano-reinforcement: A comprehensive study", *Eng. Anal. Bound. Elem.*, **146**, 598-635. https://doi.org/10.1016/j.enganabound.2022.11.014

Sobhani, E. (2023b), "Vibrational characteristic simulations regarding connecting two different semi-spheroidal shells and a full-spheroidal shell with a conical shell categorized in underwater structures", *Ocean Eng.*, **276**, 114252. https://doi.org/10.1016/j.oceaneng.2023.114252

Stankovich, S., Dikin, D.A., Dommett, G.H.B., Kohlhaas, K.M., Zimney, E.J., Stach, E.A., Piner, R.D., Nguyen, S.T. and Ruoff, R.S. (2006), "Graphene-based composite materials", *Nature*, **442**(7100), 282-286, https://doi.org/10.1038/nature04969.

Sun, L., Wang, C., Zhang, C., Yang, Z., Li, C. and Qiao, P. (2023), "Experimental investigation on the bond performance of sea sand coral concrete with FRP bar reinforcement for marine environments", *Adv. Struct. Eng.*, **26**(3), 533-546. https://doi.org/10.1177/13694332221131153

Taheri, E., Firouzianhaji, A., Mehrabi, P., Vosough Hosseini, B. and Samali, B. (2020), "Experimental and numerical investigation of a method for strengthening cold-formed steel profiles in bending", *Appl. Sci.*, **10**(11), 3855. https://doi.org/10.3390/app10113855

Taheri, E., Firouzianhaji, A., Usefi, N., Mehrabi, P., Ronagh, H. and Samali, B. (2019), "Investigation of a method for strengthening perforated cold-formed steel profiles under compression loads", *Appl. Sci.*, **9**(23), 5085. https://doi.org/10.3390/app9235085

Taheri, E., Mehrabi, P., Rafiei, S. and Samali, B. (2021), "Numerical evaluation of the upright columns with partial reinforcement along with the utilisation of neural networks with combining feature-selection method to predict the load and displacement", *Appl. Sci.*, **11**(22), 11056. https://doi.org/10.3390/app112211056

Tang, Y., Wang, Y., Wu, D., Chen, M., Pang, L., Sun, J., Feng, W. and Wang, X. (2023), "Exploring temperature-resilient recycled

aggregate concrete with waste rubber: An experimental and multi-objective optimization analysis", *Rev. Adv. Mater. Sci*., **62**(1), 20230347. https://doi.org/10.1515/rams-2023-0347

Tian, L.M., Li, M.H., Li, L., Li, D.Y. and Bai, C. (2023), "Novel joint for improving the collapse resistance of steel frame structures in column-loss scenarios", *Thin Wall. Struct*., **182**, 110219. https://doi.org/10.1016/j.tws.2022.110219

Toghroli, A., Mehrabi, P., Shariati, M., Trung, N.T., Jahandari, S. and Rasekh, H. (2020), "Evaluating the use of recycled concrete aggregate and pozzolanic additives in fiber-reinforced pervious concrete with industrial and recycled fibers", *Constr. Build. Mater*., **252**, 118997. https://doi.org/10.1016/j.conbuildmat.2020.118997

Wang, X. and Zhang, L. (2021), "Physics-informed neural networks: A deep learning framework for solving the vibrational problems", *Adv. Nano Res*., **11**(5), 495, https://doi.org/10.12989/anr.2021.11.5.495

Wang, D., Ren, B., Cui, B., Wang, J., Wang, X. and Guan, T. (2021a), "Real-time monitoring for vibration quality of fresh concrete using convolutional neural networks and IoT technology", *Auto. Constr*., **123**, 103510. https://doi.org/10.1016/j.autcon.2020.103510

Wang, P., Yuan, P., Sahmani, S. and Safaei, B. (2021b), "Surface stress size dependency in nonlinear free oscillations of FGM quasi-3D nanoplates having arbitrary shapes with variable thickness using IGA", *Thin Wall. Struct*., **166**, 108101. https://doi.org/10.1016/j.tws.2021.108101

Wang, Y., Teng, C., Hu, T. and Wang, J. (2021c), "Total conversion from graphite to few-layer graphene nanocomposite", *Carbon Trends*, **2**, 100017, https://doi.org/10.1016/j.cartre.2020.100017.

Wang, H., Zhang, X. and Jiang, S. (2022a), "A laboratory and field universal estimation method for tire–pavement interaction noise (TPIN) based on 3D image technology", *Sustainability*. **14**(19), 12066. https://doi.org/10.3390/su141912066

Wang, M., Yang, X. and Wang, W. (2022b), "Establishing a 3D aggregates database from X-ray CT scans of bulk concrete", *Constr. Build. Mater*., **315**, 125740. https://doi.org/10.1016/j.conbuildmat.2021.125740

Wang, Z., Wang, Q., Jia, C. and Bai, J. (2022c), "Thermal evolution of chemical structure and mechanism of oil sands bitumen", *Energy*, **244**, 123190. https://doi.org/10.1016/j.energy.2022.123190

Wu, J., Yang, Y., Mehrabi, P. and Nasr, E.A. (2023), "Efficient machine-learning algorithm applied to predict the transient shock reaction of the elastic structure partially rested on the viscoelastic substrate", *Mech. Adv. Mater. Struct*., 1-25. https://doi.org/10.1080/15376494.2023.2183289

Wu, M., Ba, Z. and Liang, J. (2022), "A procedure for 3D simulation of seismic wave propagation considering source-path-site effects: Theory, verification and application", *Earthq. Eng. Struct. Dyn*., **51**(12), 2925-2955. https://doi.org/10.1002/eqe.3708

Wu, Z., Huang, B., Fan, J. and Chen, H. (2023), "Homotopy based stochastic finite element model updating with correlated static measurement data", *Measurement*, **210**, 112512. https://doi.org/10.1016/j.measurement.2023.112512

Xu, L., Cai, M., Dong, S., Yin, S., Xiao, T., Dai, Z., Wang, Y. and Soltanian, M.R. (2022), "An upscaling approach to predict mine water inflow from roof sandstone aquifers", *J. Hydrol*., **612**, 128314. https://doi.org/10.1016/j.jhydrol.2022.128314

Xue-feng, L.I., Liang, K. and Mao-song, H. (2013), "Property-dependent plastic potential theory for geomaterials", *Chinese J. Geotech. Eng*., **35**(9), 1722-1729. https://doi.org/10.1016/j.cjge.2013.100035

Yang, Y. and Zhang, Q. (1997), "A hierarchical analysis for rock engineering using artificial neural networks", *Rock Mech. Rock Eng*., **30**, 207-222. https://doi.org/10.1007/BF01045717

Yang, H.Q., Zeng, Y.Y., Lan, Y.F. and Zhou, X.P. (2014), "Analysis of the excavation damaged zone around a tunnel accounting for geostress and unloading", *Int. J. Rock Mech. Min. Sci*., **69**, 59-66. https://doi.org/10.1016/j.ijrmms.2014.03.003

Yang, H.Q., Li, Z., Jie, T.Q. and Zhang, Z.Q. (2018a), "Effects of joints on the cutting behavior of disc cutter running on the jointed rock mass", *Tunnell. Undergr. Space Technol*., **81**, 112-120. https://doi.org/10.1016/j.tust.2018.07.023

Yang, H.Q., Xing, S.G., Wang, Q. and Li, Z. (2018b), "Model test on the entrainment phenomenon and energy conversion mechanism of flow-like landslides", *Eng. Geol*., **239**, 119-125. https://doi.org/10.1016/j.enggeo.2018.03.023

Yang, H., Wang, Z. and Song, K. (2020), "A new hybrid grey wolf optimizer-feature weighted-multiple kernel-support vector regression technique to predict TBM performance", *Eng. Comput*., 1-17. https://doi.org/10.1007/s00366-020-01217-2

Yang, Z., Lu, H., Sahmani, S. and Safaei, B. (2021), "Isogeometric couple stress continuum-based linear and nonlinear flexural responses of functionally graded composite microplates with variable thickness", *Arch. Civil Mech. Eng*., **21**, 1-19. https://doi.org/10.1007/s43452-021-00264-w

Yang, H., Song, K. and Zhou, J. (2022a), "Automated recognition model of geomechanical information based on operational data of tunneling boring machines", *Rock Mech. Rock Eng*., 1-18. https://doi.org/10.1007/s00603-021-02723-5

Yang, J., Fu, L.Y., Zhang, Y. and Han, T. (2022b), "Temperature- and pressure-dependent pore microstructures using static and dynamic moduli and their correlation", *Rock Mech. Rock Eng*., **55**(7), 4073-4092. https://doi.org/10.1007/s00603-022-02829-4

Yang, H., Chen, C., Ni, J. and Karekal, S. (2023), "A hyperspectral evaluation approach for quantifying salt-induced weathering of sandstone", *Sci. Total Environ*., **885**, 163886. https://doi.org/10.1016/j.scitotenv.2023.163886

Yao, W., Yu, J., Liu, X., Zhang, Z., Feng, X. and Cai, Y. (2023), "Experimental and theoretical investigation of coupled damage of rock under combined disturbance", *Int. J. Rock Mech. Min. Sci*., **164**, 105355. https://doi.org/10.1016/j.ijrmms.2023.105355

Yuan, J., Wang, T.J. and Chen, J. (2023), "Microscopic mechanism study of the creep properties of soil based on the energy scale method", *Front. Mater*., **10**, 1137728. https://doi.org/10.3389/fmats.2023.1137728

Zhang, W., Kang, S., Liu, X., Lin, B. and Huang, Y. (2023), "Experimental study of a composite beam externally bonded with a carbon fiber-reinforced plastic plate", *J. Build. Eng*., **71**, 106522. https://doi.org/10.1016/j.jobe.2023.106522

Zhen, W., Cheung, Y.K., Lo, S. and Wanji, C. (2010), "On the thermal expansion effects in the transverse direction of laminated composite plates by means of a global–local higher-order model", *Int. J. Mech. Sci*., **52**(7), 970-981. https://doi.org/10.1016/j.ijmecsci.2010.03.013.

Zhou, S., Lu, C., Zhu, X. and Li, F. (2021), "Preparation and characterization of high-strength geopolymer based on BH-1 lunar soil simulant with low alkali content", *Engineering*, **7**(11), 1631-1645. https://doi.org/10.1016/j.eng.2020.10.016

Zhou, X., Wang, P., Al-Dhaifallah, M., Rawa, M. and Khadimallah, M.A. (2022), "A machine learning-based model for the estimation of the critical thermo-electrical responses of the sandwich structure with magneto-electro-elastic face sheet", *Adv. Nano Res*., **12**(1), 81. https://doi.org/10.12989/anr.2022.12.1.081

Zhou, C., Wang, J., Shao, X., Li, L., Sun, J. and Wang, X. (2023a), "The feasibility of using ultra-high performance concrete (UHPC) to strengthen RC beams in torsion", *J. Mater. Res. Technol*., **24**, 9961-9983. https://doi.org/10.1016/j.jmrt.2023.05.185

Zhou, F., Li, W., Hu, Y., Huang, L., Xie, Z., Yang, J., Wu, D. and

Chen, Z. (2023b), "Moisture diffusion coefficient of concrete under different conditions", *Buildings*, **13**(10), 2421. https://doi.org/10.3390/buildings13102421

Zhou, T., Yu, F., Li, L., Dong, Z. and Fini, E.H. (2023c), "Swelling-degradation dynamic evolution behaviors of bio-modified rubberized asphalt under thermal conditions", *J. Clean. Prod.*, **426**, 139061. https://doi.org/10.1016/j.jclepro.2023.139061

CC